

Impact Factor: 2.25-Year Impact Factor: 2.3

Contents

PDF/EPUB

More

## Abstract

The knowledge of the temperature and particulate matter mass distribution is essential for monitoring the performance and durability of a catalyzed particulate filter. A catalyzed particulate filter model was developed, and it showed capability to accurately predict temperature and particulate matter mass distribution and pressure drop across the catalyzed particulate filter. However, the high-fidelity model is computationally demanding. Therefore, a reduced order multi-zone particulate filter model was developed to reduce computational complexity with an acceptable level of accuracy. In order to develop a reduced order model, a parametric study was carried out to determine the number of zones necessary for aftertreatment control applications. The catalyzed particulate filter model was further reduced by carrying out a sensitivity study of the selected model assumptions. The reduced order multi-zone particulate filter model with  $5 \times 5$  zones was selected to develop a catalyzed particulate filter state estimator considering its computational time and accuracy. Next, a Kalman filter-based catalyzed particulate filter estimator was developed to estimate unknown states of the catalyzed particulate filter such as temperature and particulate matter mass distribution and pressure drop ( $\Delta P$ ) using the sensor inputs to the engine electronic control unit and the reduced order multi-zone particulate filter model. A diesel oxidation catalyst estimator was also integrated with the catalyzed particulate filter estimator in order to provide estimates of diesel oxidation catalyst outlet concentrations of  $\text{NO}_2$  and hydrocarbons and inlet temperature for the catalyzed particulate filter estimator. The combined diesel oxidation catalyst–catalyzed particulate filter estimator was validated for an active regeneration experiment. The validation results for catalyzed particulate filter temperature distribution showed that the root mean square temperature error by using the diesel oxidation catalyst–catalyzed particulate filter estimator is within  $3.2^\circ\text{C}$  compared to experimental data. Similarly, the  $\Delta P$  estimator closely simulated the measured total  $\Delta P$ .

and the estimated cake pressure drop error is within 0.2 kPa compared to the high-fidelity catalyzed particulate filter model.

---

## Introduction

The diesel oxidation catalyst–catalyzed particulate filter (DOC-CPF) systems are the most commonly used aftertreatment configuration to meet EPA 2007 particulate matter (PM) emission standards along with a selective catalytic reduction (SCR) for the oxides of nitrogen (NOx) 2010/2013 emission standards. The DOC is a flow through device and it is used to oxidize hydrocarbons (HC), NO, and CO emissions. By oxidizing NO into NO<sub>2</sub>, the oxidation of PM in the CPF (NO<sub>2</sub>-assisted oxidation) results in passive oxidation of the PM retained in the CPF. The DOC also acts to oxidize fuel dosed in upstream of the catalyst, in order to increase the temperature of the exhaust gas into the CPF for active regeneration of the particulate filter. The knowledge of PM mass retained as function of a time is the vital input for an effective and efficient active regeneration strategy. The current engine electronic control unit (ECU) controls the PM loading using an internal empirical PM estimator model. The PM estimator model relies on the calibrated engine maps, pressure drop across the CPF, and temperature measurements to determine PM mass retained and regeneration frequencies.<sup>1</sup> Advanced regeneration strategies use simplified CPF models that run real time within the ECU to provide more accurate feedback on current PM loading of the filter substrate. By applying simplified models that are similar to the ones used during design, development and application of CPFs, the regeneration frequency and duration can be optimized based on vehicle operating conditions which determine engine operating conditions. This would lead to reducing fuel consumption, reducing CO<sub>2</sub> emissions, and increasing the durability of the CPF.

The heavy-duty emission regulations require on-board diagnostics (OBD) to monitor the performance of the emission control system during in-use vehicle operating conditions. The  $\Delta P$ , temperature, and PM mass retained distribution are the key performance indicators of the CPF condition. The  $\Delta P$  from a simplified model is necessary for developing an ECU-based state estimator that uses the vehicle on-board experimentally measured  $\Delta P$  along with the estimated  $\Delta P$  from the model. This is because the model can breakdown the components of the  $\Delta P$ , so appropriate control action can be taken. Therefore, the main objective of this research is to develop a computationally efficient CPF state estimator that runs fast enough

(model run time faster than real time, that is, real-time factor <1) in the engine ECU to predict temperature and PM loading distribution and pressure drop of the CPF. This goal is accomplished by using the results from a high-fidelity CPF model to develop a reduced order MPF model for the purpose of CPF state estimation. The detailed high-fidelity model and results are presented in Mahadevan et al.<sup>2,3</sup> The development of reduced order model and CPF estimator is presented in this work. The specific contributions of this work are as follows:

1. Carry out a parametric study to determine the required number of zones in a reduced order multi-zone particulate filter (MPF) model for aftertreatment control applications;
2. Develop a reduced order model to
  - Predict temperature distribution, PM mass retained distribution, and  $\Delta P$  across filter.
3. Develop an extended Kalman filter (EKF)-based two-dimensional (2D) CPF state estimator that uses the DOC model outlet NO<sub>2</sub> concentration and real sensor data to
  - Estimate temperature distribution, PM mass retained distribution, and  $P$  across filter.
4. Evaluate the performance of the DOC-CPF state estimator compared to the high-fidelity model and the experimental data.

## Literature review: Kalman filter–based state estimators for exhaust aftertreatment systems

The Kalman filter is a widely used method for tracking and estimation of state variables due its simplicity, optimality, and robustness. It is a recursive filter that can optimally estimate the states of the linear system taking into account the system dynamics and inputs.<sup>4</sup> An EKF is the non-linear version of the Kalman filter and retains the linear covariance and gain matrices; however, it uses the non-linear state propagation equations and output vector. The unique feature of the Kalman filter is that it incorporates the measurements and measurement error statistics (approximated as Gaussian) in the state variable estimate. It finds the stochastic relations between the model and sensor measurements and then estimates the system states in an optimal approach.

Kalman filter-based digital control techniques were explored by several researchers for optimal control of the engine and DOC-diesel particulate filter (DPF)-SCR-based aftertreatment systems. Chauvin et al.<sup>5</sup> developed an air–fuel ratio (AFR) estimator from a global oxygen sensor measurement using the time-varying Kalman filter model. Their work demonstrated the closed loop control of AFR for combustion control applications. Tschanz et al.<sup>6</sup> proposed a control scheme that integrates the feedback of the engine-out emissions of NOx and PM for effective engine-out emission control. This controller scheme used the model-based observer to overcome the slow dynamics of the sensors (NOx and PM). The production-type PM sensor was not available during this study. Hence, an AVL Micro Soot Sensor was used as a substitute for the production-type PM sensor. This emission controller reduced the variations in emission outputs due to the drift and transient operating conditions. The sensor measurement of engine-out NOx is the key input for the emission control of SCR aftertreatment systems. Hsieh and Wang<sup>7</sup> developed an EKF-based estimator to improve the accuracy of the NOx sensor measurement for SCR control applications.

Guardiola et al.<sup>8</sup> developed an online adaptive algorithm for updating the NOx look-up tables used in the SCR control applications. This adaptive algorithm used simplified Kalman filtering due to its capability for tracking the system and parameters during aging. Surenahalli et al.<sup>9</sup> developed an EKF-based estimator for NH<sub>3</sub> storage, NO, NO<sub>2</sub>, and NH<sub>3</sub> estimation in SCR control applications without a ammonia oxidation catalyst to aid OBD strategies to detect system failure modes. Furthermore, Surenahalli et al.<sup>10,11</sup> and Surenahalli<sup>12</sup> developed an EKF-based DOC estimator to estimate the internal states of the DOC such as CO, NO, NO<sub>2</sub>, and C<sub>3</sub>H<sub>6</sub> concentrations and temperatures in the catalyst. The estimator used the single outlet temperature measurement, in combination with the inlet concentrations of CO and HC, inlet exhaust gas temperature, exhaust mass flow rate, and the NOx concentrations from a NOx sensor. In addition, the estimator assumed the NO<sub>2</sub>/NOx ratio of 0.1 to estimate the engine outlet NO and NO<sub>2</sub> concentrations from the NOx sensor signals.

In continuation with the aforementioned efforts, this research focuses on development of a CPF estimator to function with a DOC estimator in order to predict CPF states such as PM mass retained, temperature, and PM mass retained distribution within the CPF and the pressure drop across the CPF for active regeneration control purposes. The temperature distribution within the filter substrate is non-uniform and varies axially and radially.<sup>13</sup> The non-uniform temperature distribution results in non-uniform PM mass distribution which affects the overall pressure drop of the CPF. Most researchers<sup>14</sup> applied simplified one-dimensional (1D) models for the real-time estimation of PM mass loading, whereas this

research presents the approach for the real-time estimation of 2D temperature and PM mass distribution along with the pressure drop using the 2D reduced order model equations. This approach has the potential for optimizing the regeneration time and interval based on the PM loading and temperature at various axial and radial positions within the CPF. To the best of authors' knowledge, *this is the first study undertaken to develop a real-time EKF-based estimator that includes combined estimation of 2D temperature and PM mass distribution of a CPF along with the pressure drop using the 2D reduced order model equations.* In addition, this is an extension for application of a Kalman filter in diesel engine aftertreatment systems.

## Experimental data

The experimental study was carried out on a Cummins 272 kW 2007 ISL engine with DOC and CPF aftertreatment components. Experimental data, collected by Shiel et al.<sup>15</sup> and Pidgeon et al.<sup>16</sup> at 18 different operating conditions, were used to calibrate the high-fidelity model developed in Mahadevan et al.<sup>2,3</sup> The specifications of the engine and aftertreatment system are shown in [Tables 1](#) and [2](#), respectively. The summary of the 18 test runs used to calibrate the high-fidelity model is shown in [Table A.1](#) (six passive oxidation experiments) and [Table A.2](#) (12 active regeneration experiments) in Appendix A of Supplementary Material. The experiments were performed with three diesel fuels including ULSD, B10, and B20 blends. The properties of test fuels used for the experiments are documented in Shiel et al.<sup>15</sup> and Pidgeon et al.<sup>16</sup>

**Table 1.** Specifications of engine.<sup>15,16</sup>

Model	Cummins ISL
Year of manufacture	2007
Cylinders	6, inline
Bore × stroke	115 × 144.5 mm
Displacement volume	8.9 L

Aspiration	Turbocharged
Aftercooling	Charge air cooler
Rated power	272 kW @ 2100 r/min
Peak torque	1695 N m @ 1400 r/min
EGR system	EGR system electronically controlled and cooled

EGR: exhaust gas recirculation.

**Table 2.** Specifications of the aftertreatment system used in the experiments.<sup>15,16</sup>

	DOC	CPF	Units
Substrate material	Cordierite	Cordierite	–
Cell geometry	Square	Square	–
Catalyst type	Noblemetal-based oxidation catalyst	Noblemetal-based oxidation catalyst	
Diameter	267	267	mm
Length	102	305	mm
Total volume	5.7	17.1	L
Number of cells per unit area	62 (400)	31 (200)	cells/cm <sup>2</sup> (cells in <sup>-2</sup> )
Cell width	1.09	1.49	mm
Frontal area	81	69	%
annel wall thickness	0.114	0.305	mm

	DOC	CPF	Units
Wall density	NA	0.45	g/cm <sup>3</sup>
Specific heat	NA	891	J/kg/K
Thermalconductivity	NA	0.84	W/m/K
Porosity	35	52	%
Mean pore size	NA	13	μm

DOC: diesel oxidation catalyst; CPF: catalyzed particulate filter.

The material property data (specific heat, thermal conductivity, and porosity) listed in [Table 2](#) were obtained from the supplier. In order to account for any uncertainties associated with the supplier data, the model calibration procedure explained in Mahadevan<sup>17</sup> includes calibration of the thermal (thermal conductivity, heat transfer coefficients) and physical (substrate density, clean wall permeability) properties of the filter to closely simulate the experimental temperature distribution and pressure drop of the filter.

### Passive oxidation experiments

An overview of the passive oxidation experimental test procedure is shown in [Figure 1](#). The passive oxidation experiment starts with the CPF clean out phase where the engine was operated at active regeneration test condition (600 °C for 15 min to clean out the PM in the CPF) followed by stage 1 loading of filter with a DOC inlet temperature of 265 °C ± 10 °C for 30 min. Then the stage 2 loading starts after weighing of the filter at the end of stage 1. The engine operating conditions for stage 2 loading are the same as stage 1. The stage 2 loading continues to achieve a target filter loading of 2.2 ± 0.2 g/L. At the end of stage 2 loading, the filter was weighed again and the test was continued further with the ramp up (RU) condition for 15 min before switching to the passive oxidation stage to achieve a stable filter temperature for PM oxidation. The engine operating conditions for the RU condition are the same as those in stages 1 and 2 loading conditions. During stage 2 CPF weighing process, the temperature decreases and hence, after reinstalling the CPF in the engine, the engine is operated at RU condition before switching to the passive oxidation stage. Following the

RU condition, the engine was operated at the passive oxidation test conditions (engine speed and load at which there is a significant PM, NO<sub>2</sub>/NOx ratio and temperatures >300 °C) for a pre-determined duration and at the temperatures listed in [Table A.1](#) in Appendix A of Supplementary Material. Upon completion of the passive oxidation phase, the engine was operated at stage 3 loading conditions (engine conditions are the same as stage 1 and 2) for 30 min and then the filter was weighed to determine the filter weight. Then the test was continued further with stage 4 loading for 60 min and then the filter was weighed again to determine the post-loading weight of the filter.

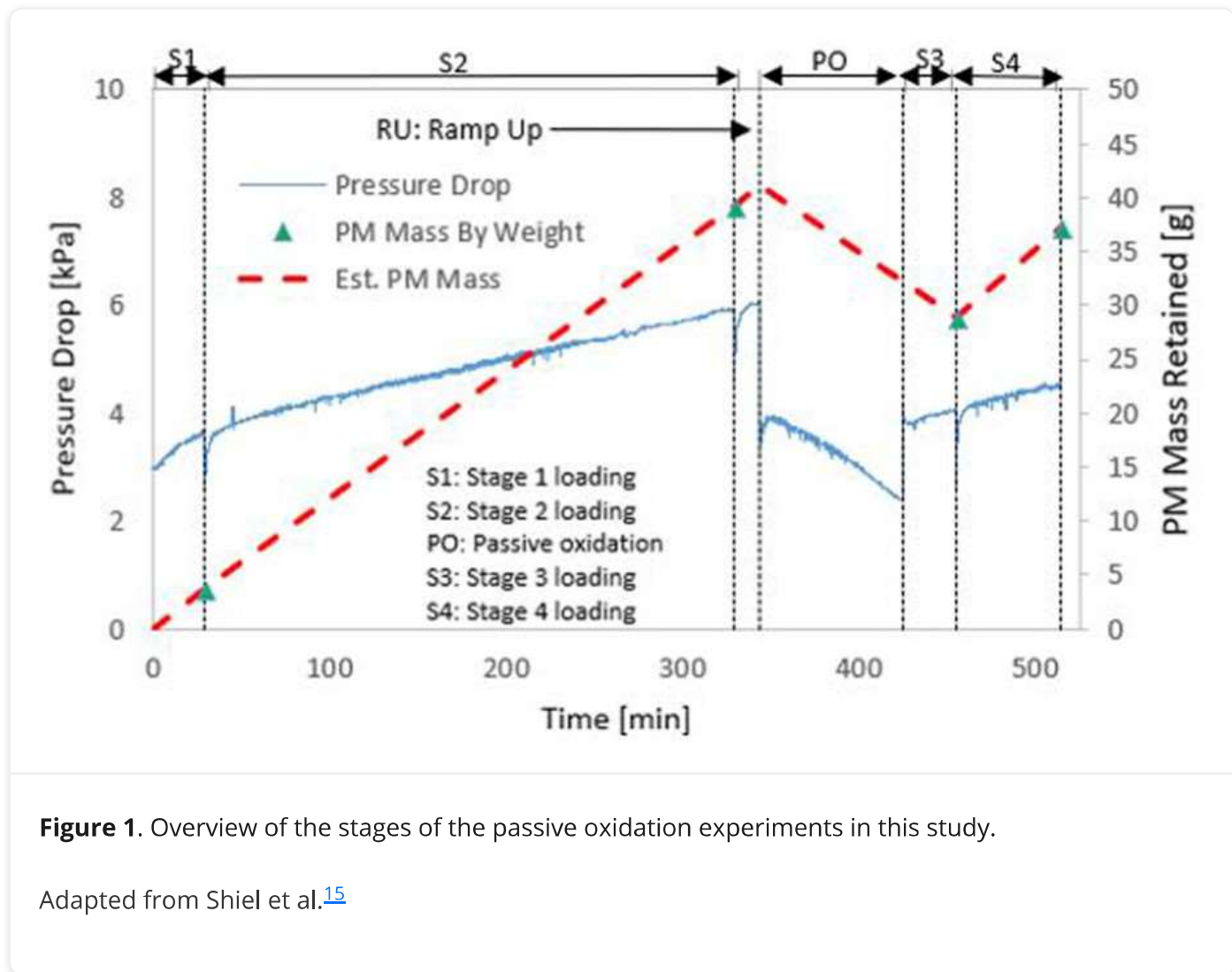


**Figure 1.** Overview of the stages of the passive oxidation experiments in this study.

Adapted from Shiel et al.[15](#)

### Active regeneration experiments

An overview of active regeneration experimental test procedure is shown in [Figure 2](#). The CPF clean out phase, stage 1–2 loading, RU of 15 min, and stage 3–4 loading are similar to passive oxidation experimental data. In the RU, the engine was operated at stage 2 loading conditions for 15 min or until the DOC inlet temperature has stabilized at 265 ± 10 °C

and then the active regeneration ramp phase for 10 min or until the DOC inlet temperature has stabilized at  $325 \pm 10$  °C to stabilize the CPF temperature prior to active regeneration. The active regeneration stage was continued for a pre-determined amount of time at the specified CPF inlet temperatures listed in [Table A.2](#) in Appendix A of Supplementary Material. If the active regeneration was allowed to continue for a longer period of time other than the specified durations in [Table A.2](#), then there would not be enough PM within the CPF to obtain an accurate PM mass retained measurement. The experimental data (temperature distribution, PM loading, filtration efficiency, and  $\Delta P$ ) from the AR-B10-1 active regeneration experiment is used in this study for the validation of the DOC-CPF estimator.

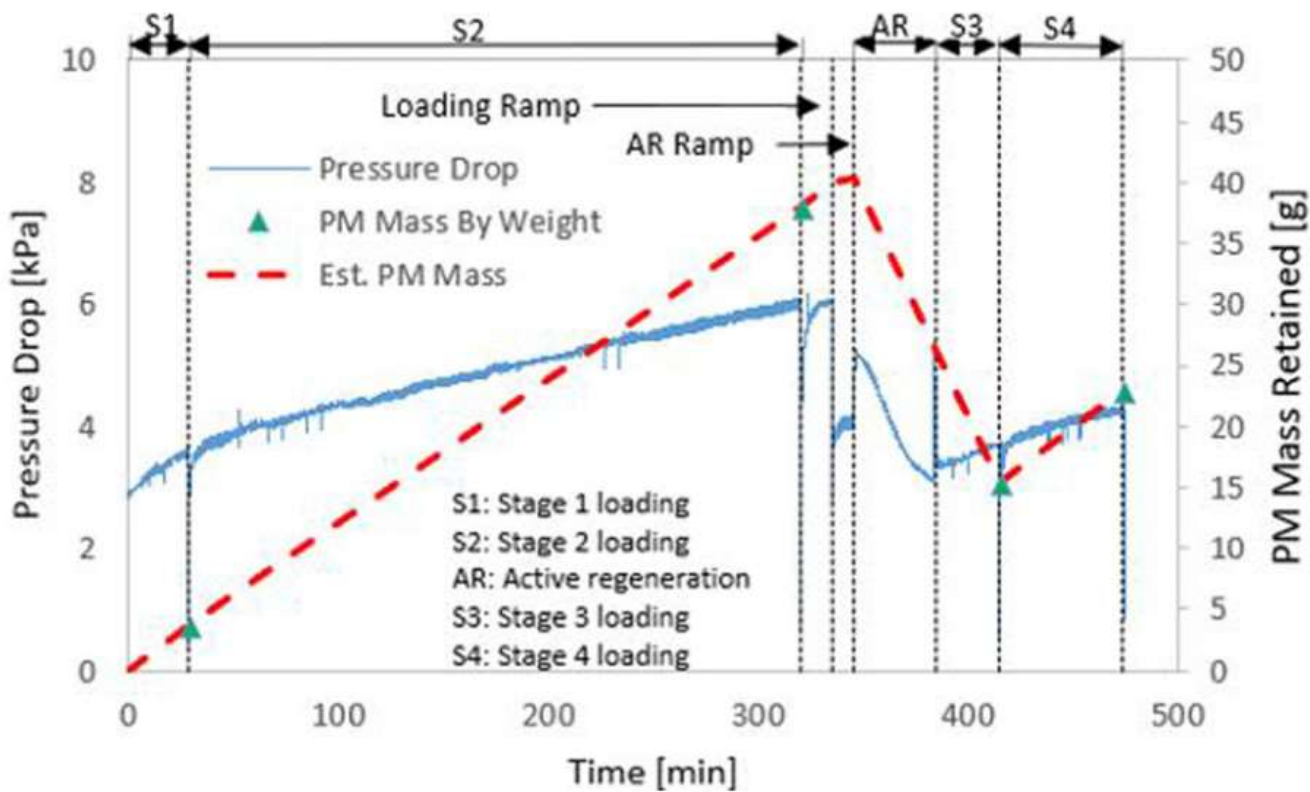


**Figure 2.** Overview of the stages of the active regeneration experiments in this study.

Adapted from Pidgeon et al.[16](#)

### CPF temperature distribution

The experimental gas temperature distribution data recorded in Shiel et al.[15](#) and Pidgeon et al.[16](#) is used to validate the DOC-CPF estimator from this work. The CPF thermocouple layout and for the gas temperature distribution measurements is shown in [Figure 3](#). The K-type

thermocouples with the diameter of 0.81 mm were used for this temperature distribution measurement.

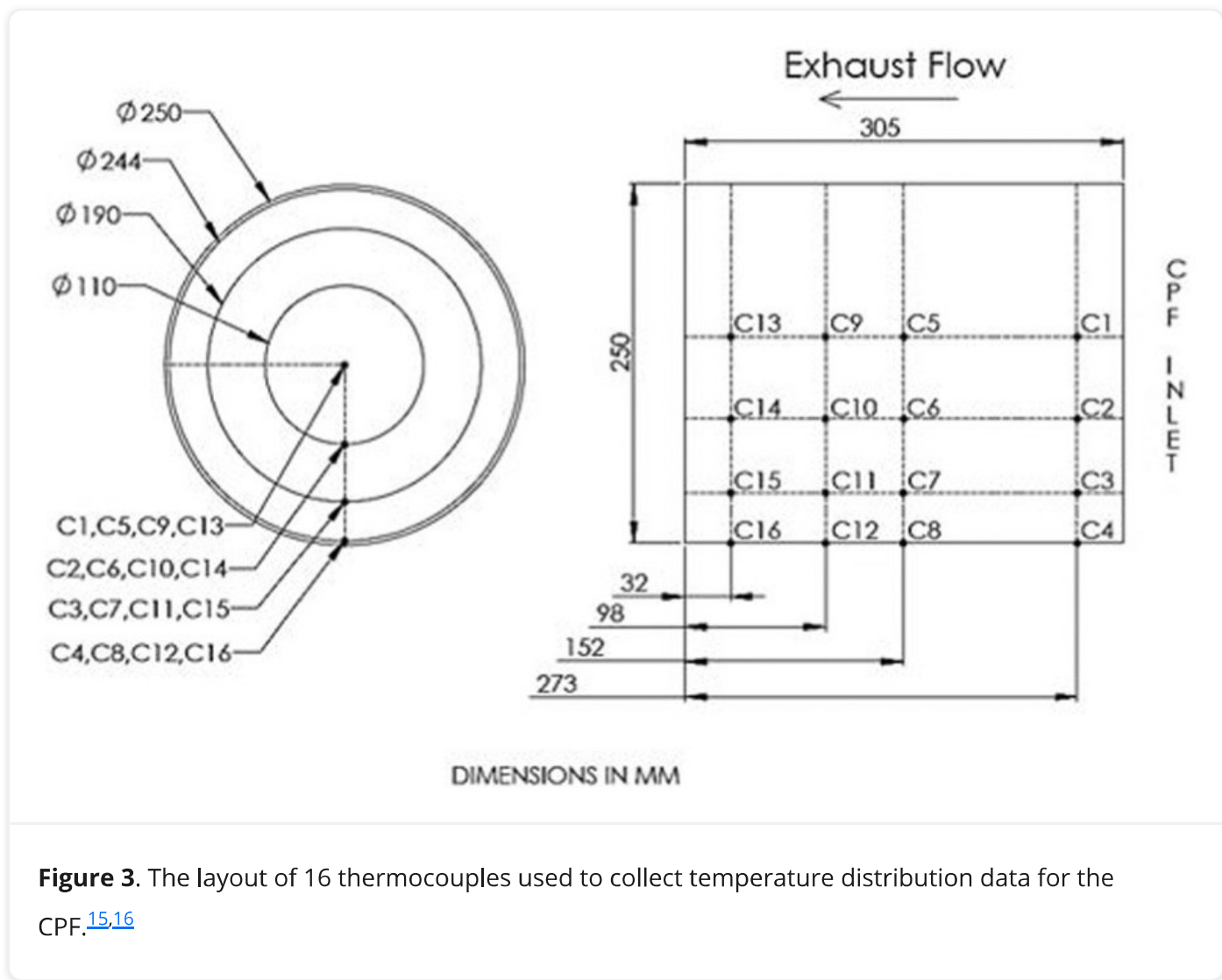


**Figure 3.** The layout of 16 thermocouples used to collect temperature distribution data for the CPF.[15,16](#)

## High-fidelity model overview

The high-fidelity model developed in Mahadevan et al.[2,3](#) is used in this research for the development and validation of the reduced order model and CPF state estimator. In the high-fidelity model, the CPF is divided into user configurable number of axial and radial zones as shown in [Figure 4](#). The results from a  $10 \times 10$  zone high-fidelity model were used in this work to compare with the reduced order model and CPF estimator. A brief overview of the high-fidelity model is presented in this section and detailed model and validation with experimental data are available in Mahadevan et al.[2,3](#)

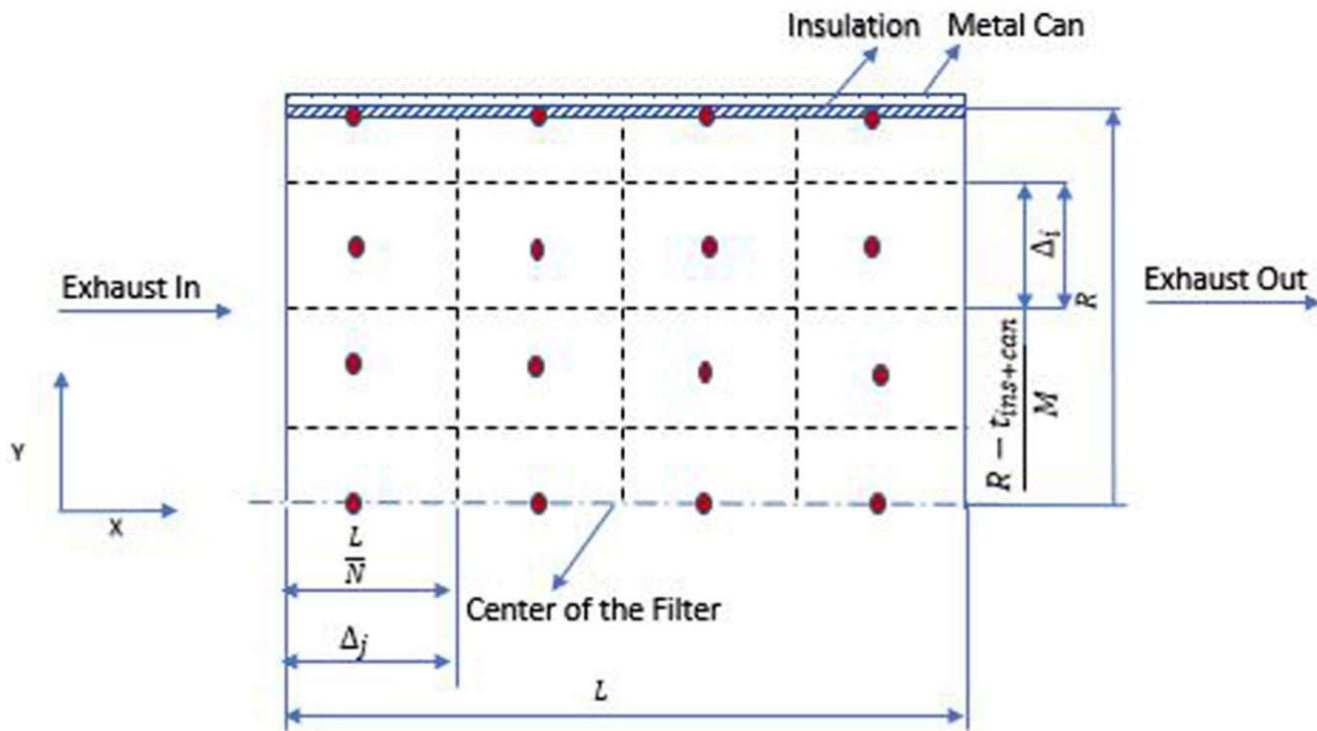


**Figure 4.** Schematic of a high-fidelity CPF model shown for a sample  $4 \times 4$  zonal distribution.<sup>3</sup>

The filter and gas energy equation is employed at each zone. The model takes into account inlet temperature distribution assuming the fully developed boundary layer at the inlet of the CPF. The model accounts for the PM filtration and oxidation within the substrate wall and PM cake separately in each zone along with the cake permeability. The PM oxidation includes PM oxidation by thermal ( $O_2$ ) and  $NO_2$ -assisted mechanisms using inlet  $O_2$  and  $NO_2$  concentrations. In addition to the model developed in Mahadevan et al.,<sup>23</sup> the chemical species solver was developed and applied at each zone to account for reactions in the catalyst washcoat and substrate wall. The reactions ( $\dot{Q}_{\text{reac,PM}}$ ,  $\dot{Q}_{\text{reac,HC}}$ ) in the catalyst washcoat and substrate wall provide additional  $NO_2$  for PM oxidation. Hence, the PM oxidation equations account for the back diffusion of the  $NO_2$  into the PM cake layer. The model also accounts for the HC emissions oxidation which is assumed to occur within the filter. The pressure drop across the filter was calculated using the packed bed filtration theory.<sup>18</sup> The pressure drop model used in the CPF model accounts for the PM filtration in the wall and cake, variable wall and cake permeability, the changes in the mean-free path length of the gas and permeability evolution of PM cake during PM oxidation and post-cleaning using the recently developed cake permeability model.<sup>3</sup> The outputs of the high-fidelity CPF model are temperature distribution within the filter substrate, inlet and outlet

channels, total PM mass retained including masses in the cake and wall, PM loading distribution within the filter, species concentration at the filter outlet (NO, NO<sub>2</sub>, CO, CO<sub>2</sub>, O<sub>2</sub>, HC, and PM concentration), and pressure drop across the filter.

## Reduced order model development

The high-fidelity model developed in Mahadevan et al.<sup>2,3</sup> was simplified for using with state estimator in order to improve its computational speed and reduce the computational complexity without significantly affecting the accuracy of predicting the temperature and PM mass distribution and pressure drop of the CPF.

To develop a reduced order MPF model, the following parametric study was carried out using the high-fidelity model to determine optimum model configuration for the reduced order MPF model. To this end, a five-step process is applied:

*Step I.* The number of axial and radial zones required to predict temperature and PM mass distribution and pressure drop of the CPF for aftertreatment control applications was determined.

Furthermore, the following model reduction assumptions were evaluated using the high-fidelity CPF model to determine the sensitivity of these assumptions to the computational time and modeling inaccuracies:

*Step II.* Not applying the species concentration solver and assuming uniform species (HC, NO<sub>2</sub> and O<sub>2</sub>) concentration at each zone.

*Step III.* Neglecting the back diffusion of NO<sub>2</sub> due to the NO<sub>2</sub> produced by the catalyst washcoat.

*Step IV.* Applying average channel gas temperature assumption (i.e. neglecting the temperature change through the substrate wall).

*Step V.* Neglecting the radiation heat transfer within the inlet channel surfaces (i.e. radiation heat transfer is minimum below 600 °C).

The results of parametric study and model reduction assumptions are presented in this section.

Cell discretization study

A parametric study was carried out to determine the required number of zones in the reduced order MPF in the range of  $4 \times 4$  to  $10 \times 10$  zones for aftertreatment control applications. The filter substrate temperatures during active regeneration ( $450\text{--}600^\circ\text{C}$ ) are higher than the passive oxidation ( $250\text{--}400^\circ\text{C}$ ). The high temperatures during active regeneration result in a greater temperature distribution (AR-B10-1 experiment: average temperature during active regeneration:  $530^\circ\text{C}$ , radial temperature distribution  $\cong 40^\circ\text{C}$ , axial temperature distribution  $\cong 12^\circ\text{C}$ ) and highly non-uniform PM distribution within the filter. Hence, the active regeneration experiment AR-B10-1 was used as a reference experiment for the reduced order model development and DOC-CPF state estimator validation.

A variable step solver based on *ode15s* stiff solver was used to solve the temperature, PM distribution, and pressure drop at each time step. The maximum time step was set to 10 s and minimum time step was set to  $1\text{e}{-}8$  s to achieve numerical stability<sup>19</sup> of the model. The total test duration was approximately 7.33 h (440 min) for AR-B10-1 experiment. The model execution time was compared with real time using the real-time factor. The real-time factor is calculated as the ratio of model run time to the real time of the experiment. The real-time factor of 1 indicates that the model runs as fast as real time.

[Figure 5](#) shows the model discretization size versus real-time factor for the AR-B10-1 experiment. From [Figure 5](#), the real-time factor significantly increases with increasing the discretization size. In addition, the real-time factor increases linearly as a function of total number of zones (16 nodes for  $4 \times 4$  model, 25 nodes for  $5 \times 5$  model, 49 nodes for  $7 \times 7$  model, and 100 nodes for  $10 \times 10$  model). The lowest real-time factor is for the  $4 \times 4$  zone model in which the high-fidelity model takes 2.3% of total real time or about 43 times faster than the real time. The  $5 \times 5$  zone model takes 3.5% of total real time or about 29 times faster than the real time, whereas the baseline  $10 \times 10$  zone model takes 12.9% of total real time or about eight times faster than real time. It is important to note that the CPF model was run on a laptop computer with the specifications of 12 GB RAM, 64 bit and Intel core i7 processor. The typical ECUs used on engine applications have 32 bit and 150 MHz processors.<sup>20</sup> However, MATLAB® is the high-level programming language and it is approximately  $10\times$  slower than the C language that closely mirrors the assembly language that ECU processors commonly use. Depcik and Assanis<sup>21</sup> showed that for a sample problem, C code runs  $18.1\times$  faster than the MATLAB code. Hence, with an optimized C code, the CPF model with low computational requirement like the  $4 \times 4$  and  $5 \times 5$  zone shows high potential to run as part of a conventional ECU or a dedicated ECU that manages CPF functions exclusively.

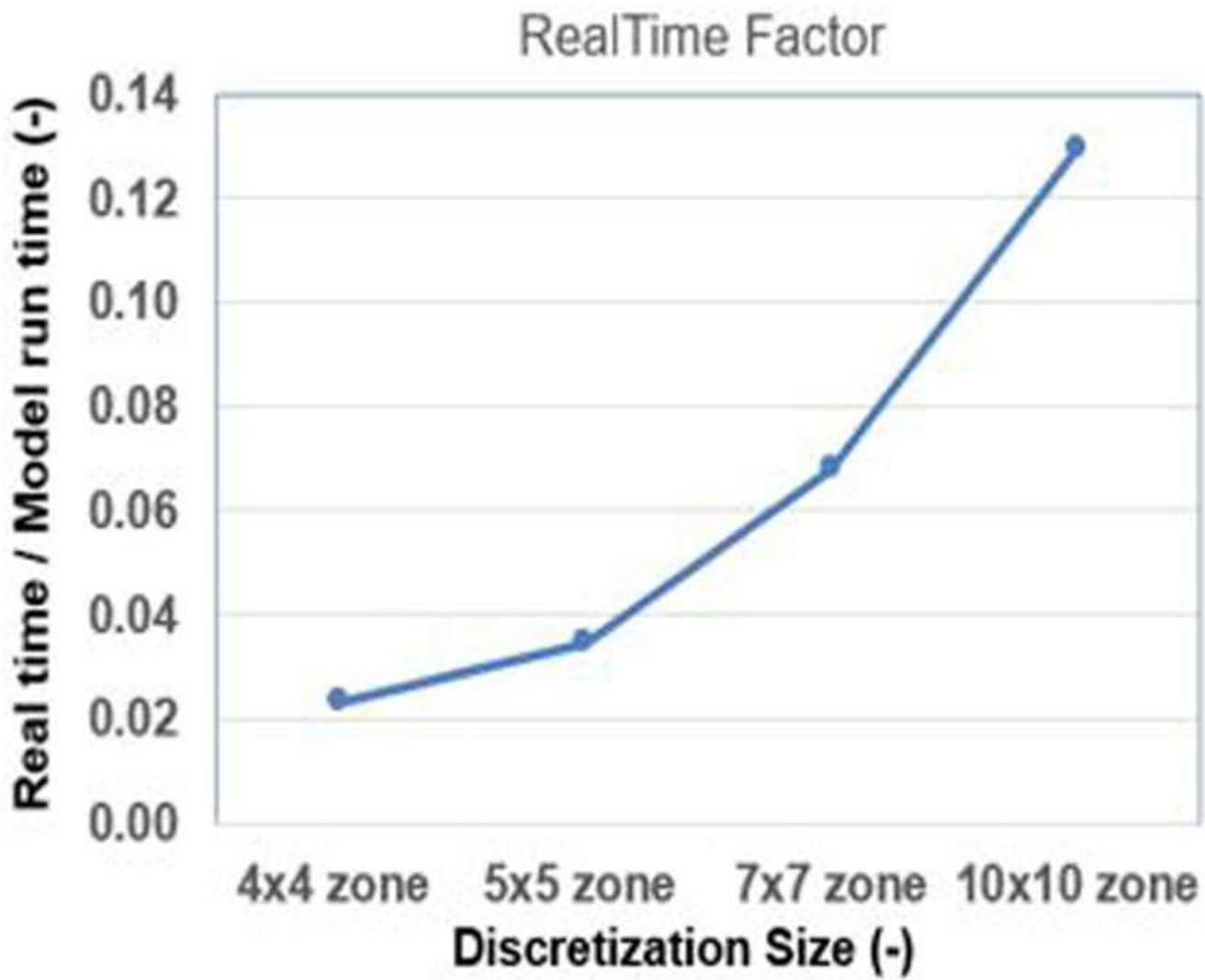


**Figure 5.** Real-time factor versus model discretization size for AR-B10-1 experiment.

Furthermore, the model predictions of temperature and PM mass distribution and pressure drop values at  $7 \times 7$ ,  $5 \times 5$ , and  $4 \times 4$  zone models were compared with the  $10 \times 10$  zone model. For the sake of brevity, a summary table for  $10 \times 10$ ,  $7 \times 7$ ,  $5 \times 5$ , and  $4 \times 4$  zone models is presented. The detailed analysis and results are available in Mahadevan.<sup>17</sup> Table 3 summarizes the model accuracy versus computational time of the high-fidelity CPF model with four discretization levels. For the real-time ECU-based applications, the fastest computational time ( $\text{Simulation time}/\text{Real time} \ll 1$ ) with the acceptable level of accuracy is required. The root mean square (RMS) temperature difference of  $<5^\circ\text{C}$ , PM loading difference of  $<2\text{ g}$ , and pressure drop difference of  $<0.2\text{ kPa}$  compared to the experimental work, leading to less than 5% average relative error for model predictions. From Table 3,

the  $5 \times 5$  zone model offers the best trade-off in terms of accuracy (meets the chosen accuracy requirements) and computational time

(Simulation time / Real time =  $0.03 \ll 1$ ) compared to the  $4 \times 4$ ,  $7 \times 7$ , and  $10 \times 10$  zone models. Thus, the  $5 \times 5$  model was selected as the discretization size (about four times faster than the baseline  $10 \times 10$  model) for the CPF reduced order model development and subsequent CPF estimator development.

**Table 3.** Temperature, PM loading, pressure drop, and computational time trade-off for the CPF model.

Model discretization level	RMS temperature difference at start of PM oxidation (time: 5.6 h)	PM loading difference at end of post- loading (time: 7.3 h)	Pressure drop difference at end PM oxidation (time: 5.8 h)	Simulation time/r time
	°C	g	kPa	(-)
$4 \times 4$ zone	5.4	2.2	-0.3	0.02
$5 \times 5$ zone	3.5	1.6	-0.2	0.03
$7 \times 7$ zone	2.6	1.2	-0.1	0.07
$10 \times 10$ zone	3.1	0.3	0.0	0.13

PM: particulate matter; RMS: root mean square.

## Model reduction

The high-fidelity model was further reduced by applying assumptions to simplify the model. The following modeling assumptions were made to develop the reduced order model.

back diffusion

Catalyzed particulate filters are coated with Pt-based catalyst which is very effective in promoting oxidation reaction of NO. The NO present in the exhaust gas flows through the inlet channels of the CPF, PM cake layer, and then into the catalyst substrate wall surfaces to the outlet channels of the CPF. The Pt-based catalyst washcoat in the substrate wall oxidizes NO in the gas into NO<sub>2</sub>. Due to the concentration gradient of NO<sub>2</sub> between the PM cake layer and the substrate wall, the NO<sub>2</sub> can diffuse back into the PM cake layer and oxidize the PM cake. This phenomenon is called NO<sub>2</sub> back diffusion. Moreover, the NO<sub>2</sub> produced in the washcoat can also flow downstream and participate further in NO<sub>2</sub>-assisted wall PM oxidation in the substrate wall. Haralampous and Koltsakis<sup>22</sup> reported that the effect of NO<sub>2</sub> back diffusion on PM oxidation could be up to 30% at low temperatures. Premchand et al.<sup>23</sup> showed that the effect is 1%–4% for the passive oxidation experiments. The NO<sub>2</sub> back diffusion is most favorable in the temperature range of 300–400 °C (passive oxidation test conditions).<sup>24</sup> Hence, the effect of NO<sub>2</sub> back diffusion on cake PM oxidation for the passive oxidation experiments was studied using the high-fidelity CPF model. It was found that the NO<sub>2</sub> back diffusion effect is within 0.1 g of PM oxidized in all passive oxidation experiments.<sup>17</sup> At higher temperatures of 400 °C–600 °C (active regeneration test conditions), NO<sub>2</sub> is not favored due to the chemical equilibrium limitation.<sup>24</sup> Hence, the NO<sub>2</sub> back diffusion was neglected in the reduced order model which is intended for aftertreatment control applications. To determine the effect of NO<sub>2</sub> back diffusion on PM oxidation for the engine studied (cooled exhaust gas recirculation (EGR) with DOC) in this research, the engine operating conditions with NO<sub>2</sub> concentrations of 61–11 ppm ( $(NO_2/NO_x) \cong 0.31 - 0.52$ ) and CPF inlet temperatures of 253–408 °C as shown in [Table A.1](#) (Appendix A of Supplementary Material) were tested. The contribution of the NO<sub>2</sub> back diffusion on the PM mass oxidation can be higher for other engine configurations such as non-EGR engines with high levels of engine out NO<sub>x</sub>, washcoat formulations, and test cycles such as federal test procedure (FTP) and ramped mode cycle (RMC) with wide range of exhaust gas temperatures and concentrations. In such cases, the reduced order model needs to account for the NO<sub>2</sub> back diffusion effect using the species concentration solver to reduce the PM oxidation modeling errors. This could add further computational time and complexity to the state estimator as explained in section “Development of Kalman filter–based CPF state estimator” of this research. Alternatively, simplified concentration tables as a function of CPF inlet temperature and gas flows can be applied in the ECU to reduce computational time and complexity at the expense of model accuracy.

## Species concentration

For the purpose of reducing the computational time for the aftertreatment control applications, the high-fidelity model was evaluated by assuming that the species concentration at each zone (wall and cake) is same as the inlet species concentration. This means the effect of catalytic reactions in the washcoat is minimum on the cake and wall PM oxidation and could be neglected (without need for using species solver) for the reduced order model. With this assumption, the model run time was 32 times faster without significantly reducing the accuracy (RMS temperature error < 2.9 °C, pressure drop error is within 0.1 kPa, and PM loading error is within 0.2 g).

#### Average channel gas temperature

Based on high-fidelity model study for the AR-B10-1 experiment, the temperature difference between inlet channel and outlet channel is minimum (absolute difference is <2 °C and RMS temperature difference is within 1 °C during PM oxidation by active regeneration) because of the high rate of convection heat transfer between the channels and the porous substrate wall. Hence, for the purpose of the reduced order model development, the lumped model approach<sup>25</sup> is employed by applying the average channel gas temperature for calculation of convection heat transfer between channels and the filter substrate. With the average channel gas temperature assumption, the temperature of the gas flow through the substrate wall can be neglected.

#### Radiation within inlet channels

The high-fidelity CPF model assumes the channel gas transmits thermal radiation to the black channel surfaces. The effect of internal radiation is very small at lower temperatures. However, this could be more important for temperatures over 600 °C and could improve the model accuracy during uncontrolled regeneration events.<sup>26</sup> Most of the operating conditions in the CPF are below 600 °C. Hence, the radiation heat transfer between channel gas and filter wall was neglected. The detailed analysis and results are available in Mahadevan.<sup>17</sup>

#### Reduced order model equations

From the discretization study in section “Model discretization study” and the model reduction study presented in section “Model reduction,” a reduced order  $5 \times 5$  zone MPF model was developed. The reduced order model governing equations with the model reduction assumptions discussed in section “Model reduction” are presented in this section.

#### Temperature model

The energy equation used for calculating the filter substrate temperature is given as follows

$$\left( \rho_s c_s V s_{i,j} + \rho_f c_f V_{f_{i,j}} \right) \frac{dT f_{i,j}}{dt} = \dot{Q}_{cond.\text{axial}} + \dot{Q}_{cond.\text{radial}} + \dot{Q}_{conv} + \dot{Q}_{reac,PM} - \quad (1)$$



where,  $T f_{i,j}$  is the filter substrate temperature at each zone,  $\rho_s$  is the density of PM cake,  $c_s$  is the specific heat of the PM cake,  $V s_{i,j}$  is the volume of PM cake in each zone,  $\rho_f$  is the filter substrate density,  $c_f$  is the specific heat of the filter substrate material,  $V_{f_{i,j}}$  is the volume of the filter in each zone,  $\dot{Q}_{cond.\text{axial}}$  is the heat transfer rate along the length of the filter,  $\dot{Q}_{cond.\text{radial}}$  is the heat transfer rate along the radial direction of the filter,  $\dot{Q}_{conv}$  is the heat transfer rate between the filter and channel gas calculated using the average channel gas temperature,  $\dot{Q}_{reac,PM}$  is the energy released during the oxidation of the PM within the filter, and  $\dot{Q}_{reac,HC}$  is the energy released during oxidation of the HC in the inlet channel gas. The species concentrations ( $O_2$ ,  $NO_2$ , and HC) used for calculating  $\dot{Q}_{reac,PM}$  and  $\dot{Q}_{reac,HC}$  are assumed to be uniform in each zone and equal to the inlet concentration. The energy equation at the outer most zones include heat transfer between metal can, insulation and the external ambient. The detailed formulation of terms used in [equation \(1\)](#) is explained in Mahadevan et al.<sup>2</sup>

### PM filtration model

The overall efficiency of the filtration is given as follows

$$\eta_{total,i,j} = 1 - \left[ \left( 1 - \eta_{cake,i,j} \right) \prod_{n=1}^{n_{\max}} \left( 1 - \eta_{wall,i,j \text{ slab } n} \right) \right] \quad (2)$$

where  $\eta_{cake,i,j}$  is the PM cake layer filtration efficiency,  $\eta_{wall,i,j \text{ slab } n}$  is the filtration efficiency of each slab in the substrate wall, and  $n_{\max}$  is the number of slabs in the substrate wall at each zone. The detailed formulation of terms used in [equation \(2\)](#) is available in Mahadevan et al.<sup>3</sup>

### oxidation model

The oxidation of PM in the cake layer is given as follows

$$\frac{d(mc_{i,j})}{dt} = -\frac{s_p \rho_{i,j} Y_{i,j,O_2} k_{O_2 i,j} W_c}{\alpha_{O_2} W_{O_2} \rho_s} mc_{i,j} - \frac{s_p \rho_{i,j} Y_{i,j,NO_2} k_{NO_2 i,j} W_c}{\alpha_{NO_2} W_{NO_2} \rho_s} mc_{i,j} \quad (3)$$

where  $mc_{i,j}$  is the PM mass in the PM cake layer at each zone,  $s_p$  is the specific surface area of PM,  $\rho_{i,j}$  is the density of the gas at each zone,  $Y_{i,j,O_2}$  is the mass fraction of inlet O<sub>2</sub> at each zone,  $Y_{i,j,NO_2}$  is the mass fraction of inlet NO<sub>2</sub> at each zone,  $k_{O_2 i,j}$  is the reaction rate constant for thermal (O<sub>2</sub>) PM oxidation,  $k_{NO_2 i,j}$  is the reaction rate constant for the NO<sub>2</sub>-assisted PM oxidation,  $W_c$  is the molecular weight of the carbon,  $W_{O_2}$  is the molecular weight of the oxygen,  $W_{NO_2}$  is the molecular weight of the NO<sub>2</sub>,  $\alpha_{O_2}$  is the O<sub>2</sub> oxidation partial factor, and  $\alpha_{NO_2}$  is the NO<sub>2</sub> oxidation partial factor.

Similarly, the PM mass reduction due to oxidation in each slab of the substrate wall is equal to the following

$$\left[ \frac{d(mw_{i,j})}{dt} \right]_n = \left[ -\frac{s_p \rho_{i,j} Y_{i,j,O_2} k_{O_2 i,j} W_c}{\alpha_{O_2} W_{O_2} \rho_s} mw_{i,j} - \frac{s_p \rho_{i,j} Y_{i,j,NO_2} k_{NO_2 i,j} W_c}{\alpha_{NO_2} W_{NO_2} \rho_s} mw_{i,j} \right]_n \quad (4)$$

where  $[mw_{i,j}]_n$  is the PM mass in the  $n$ th slab of the substrate wall at each zone.

#### Pressure drop model

The total pressure drop across the CPF is given as follows

$$\Delta P_{CPF} = \frac{\sum_{s1}^{smax} \sum_{i=1}^{i=imax} VF_i \Delta P_{CPF,i}}{smax} \quad (5)$$

where  $\Delta P_{CPF}$  is the average pressure drop across the CPF based on different volumetric flow rates in each radial section of the CPF,  $imax$  is the maximum number of axial

discretization in the model,  $VF_i$  is the volume fraction of exhaust gas flow at each radial section of the CPF, and  $smax$  is the number of ways of obtaining the absolute pressure at the inlet of the inlet channel ( $P_1|_{i,j+1}$ ) at each radial section of the filter using the streamlines approach as explained in [Appendix B](#) of Supplementary Material. The detailed formulation of the pressure drop model is explained in Mahadevan et al.<sup>3</sup>

The pressure drop due to the substrate wall and the PM cake layer is given as follows

$$\Delta P_{\text{wall}_{i,j}} = \mu_{i,j} v_{w_{i,j}} \frac{w_s}{k_{\text{wall}_{i,j}}} \quad (6)$$

$$\Delta P_{\text{cake}_{i,j}} = \mu_{i,j} v_{s_{i,j}} \frac{w_{p_{i,j}}}{k_{\text{cake}_{i,j}}} \quad (7)$$

where  $\Delta P_{\text{wall}_{i,j}}$  is the pressure drop due to the substrate wall at each zone,  $\Delta P_{\text{cake}_{i,j}}$  is the pressure drop due to the PM cake at each zone,  $\mu_{i,j}$  is the dynamic viscosity of the exhaust gas at each zone,  $v_{w_{i,j}}$  is the velocity of gas through the substrate wall at each zone,  $v_{s_{i,j}}$  is the velocity of gas through the PM cake layer at each zone,  $w_s$  is the substrate wall thickness,  $w_{p_{i,j}}$  is the PM cake layer thickness at each zone,  $k_{\text{wall}_{i,j}}$  is the wall permeability at each zone, and  $k_{\text{cake}_{i,j}}$  is the PM cake layer permeability at each zone.

The reduced order model validation with the experimental data and the high-fidelity model is not presented here but it is available in Mahadevan.<sup>17</sup> The  $5 \times 5$  zone reduced order model was used for the CPF state estimator development in the next section “Development of Kalman filter–based CPF state estimator.” Then the validation results in comparison with the experimental data and high-fidelity model are presented.

## Development of Kalman filter–based CPF state estimator

This section describes the development of the state estimator for the CPF to predict unknown states of the CPF temperature and PM mass retained distribution and pressure of the CPF. In a linear system with Gaussian noise, the Kalman filter is optimal.<sup>27</sup> In a non-linear system, an EKF can be used, but the unscented Kalman filter and particle filter<sup>28</sup>

may give better results with additional computational cost. For ECU-based applications, the linear and EKFs provide better trade-off in terms of computational cost compared to the unscented Kalman filter and particle filters.<sup>28</sup> Hence, the designed CPF state estimator in this article uses an EKF for the estimation of the temperature and PM mass retained distribution and a linear Kalman filter (LKF) for the estimation of pressure drop across the CPF.

The reduced order  $5 \times 5$  zone MPF model presented in section “Reduced order model development” is used for the development of the CPF state estimator. A DOC state estimator developed by Surenahalli et al.<sup>11</sup> was integrated with the CPF state estimator in order to determine the CPF input variables. The main purpose of the DOC state estimator is to estimate the DOC outlet temperature and concentrations of  $\text{NO}_2$  and  $\text{C}_3\text{H}_6$  from the engine out concentrations. The DOC estimator uses the inputs from engine sensors and engine maps to estimate DOC states of DOC outlet temperature and concentrations ( $\text{NO}_2$  and  $\text{C}_3\text{H}_6$ ). The DOC outlet temperature and concentrations ( $\text{NO}_2$  and  $\text{C}_3\text{H}_6$ ) along with the other engine sensor/map inputs such as  $\Delta P$ , PM inlet, and  $\text{O}_2$  concentrations and CPF outlet temperature are used as the input conditions for the CPF state estimator as shown in [Figure 6](#). The design of EKF and LKF and the simulation of the DOC-CPF state estimator on the active regeneration experiment (AR-B10-1) are presented in this section.

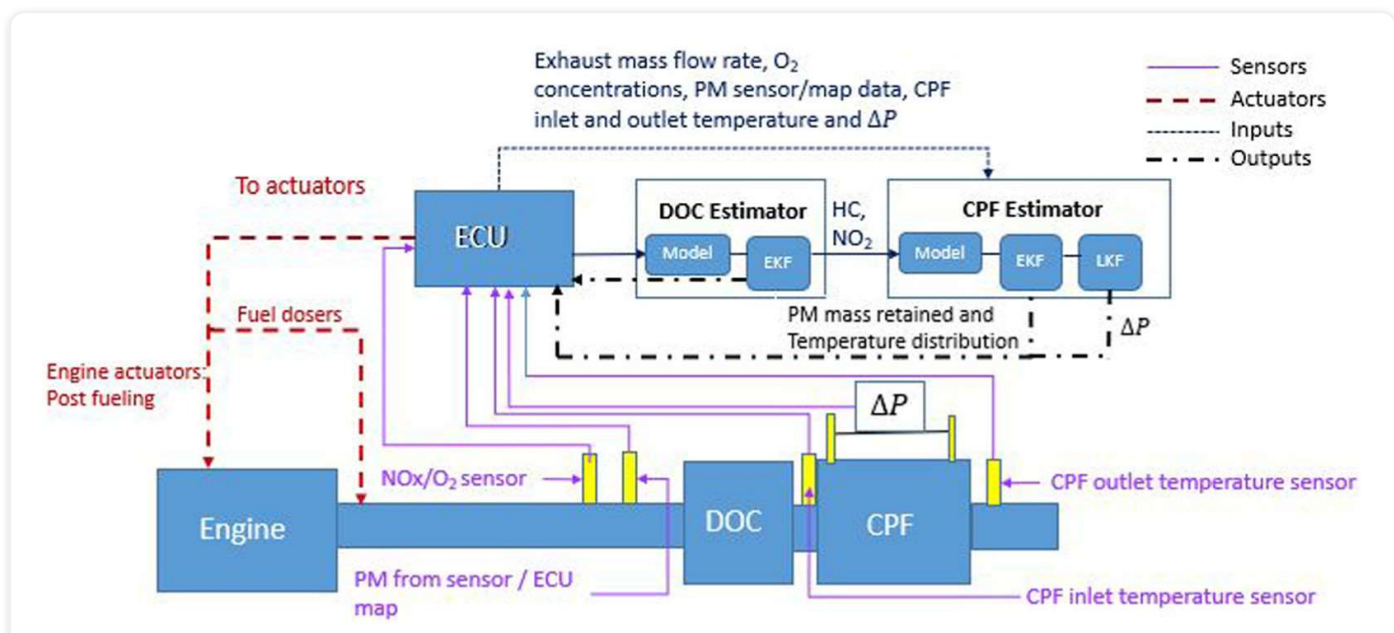


**Figure 6.** Schematic of the designed DOC and CPF estimators.

The main function of the Kalman filter is to predict the state and error covariance for the next time step based on the system model and then compensate for the difference between the measurement and prediction followed by the computation of the new estimate of the state. If the system model is non-linear, then the Kalman filter linearizes the system model with the current mean and covariance.<sup>27</sup> This type of Kalman filter is called EKF. In this work, a non-linear system model is applied ([equation \(8\)](#)) for the estimation of temperature distribution and the linear model is applied for the pressure drop estimation ([equation \(9\)](#)). The system model equation for filter temperature (Temp \_filter) distribution in a discrete form is given as follows

$$(\text{Temp\_filter}_{i,j})_k = (\text{Temp\_filter}_{i,j})_{k-1} + \frac{\dot{Q}_{\text{cond.axial } i,j} + \dot{Q}_{\text{cond.radial } i,j} + \dot{Q}_{\text{cor}}}{(\rho_s c_s V s_{i,j} + \mu)} \quad (8)$$



In [equation \(8\)](#), the filter temperature at current time is denoted with subscript  $k$  and the previous time step is denoted with subscript  $k - 1$ .

Similarly, the system model equation for the pressure drop estimation is given as follows

$$(\Delta P_{\text{Total}})_k = (\Delta P_{\text{channel}} + \Delta P_{\text{wall}} + \Delta P_{\text{cake}})_k \quad (9)$$

where  $\Delta P_{\text{channel}}$  is the channel pressure drop,  $\Delta P_{\text{wall}}$  is the substrate wall pressure drop,  $\Delta P_{\text{cake}}$  is the estimated cake pressure drop, and  $\Delta P_{\text{Total}}$  is the total pressure drop across the CPF.

### EKF for temperature distribution estimation

Here, an EKF estimator is designed to predict the unknown states of the CPF temperature distribution. The estimator output equations are used to calculate the PM mass distribution and pressure drop using the temperature states. A brief description of the state space model formulation for the EKF design is presented here. The state space representation of a discrete non-linear model with states  $x_k$ , inputs  $u_k$ , process noise  $w_k$ , and measurement noise  $v_k$  can be shown as follows

$$x_k = f_{k-1}(x_{k-1}, u_{k-1}, w_{k-1}) \quad (10)$$

$$y_k = h_k(x_k, v_k) \quad (11)$$

The CPF state estimator uses the following inputs ( $u_k$ ):

1. Instantaneous exhaust mass flow rate ( $\dot{m}$ );
2. CPF inlet concentrations (PM, NO<sub>2</sub>, O<sub>2</sub>, and C<sub>3</sub>H<sub>6</sub>);
3. CPF inlet temperature ( $T_{in,4}$ );
4. Ambient pressure and temperature

In general, noise values are estimated statistically and noise is assumed to have a normal distribution. In the EKF,  $w_k$  and  $v_k$  are assumed to be zero mean multivariate Gaussian noises with covariance  $Q_k$  and  $R_k$ , respectively.<sup>27</sup> The modeling of process noise ( $w_k$ ) is difficult and needs to be determined from the basic knowledge and experience of the system. Similarly, the measurement noise covariance ( $R_k$ ) is estimated from the error characteristics of measurement system. If both covariance matrices are difficult to obtain analytically, they can be determined by trial and error.<sup>29</sup> In this work, with the experimentally validated reduced order model, the modeling errors were assumed to be small compared to the measurement error. Hence, the process noise ( $w_k$ ) was neglected and the covariance matrix ( $R_k$ ) was constructed using the covariance of 0.1 for the measurement/observation noise ( $v_k$ ) based on the earlier reference.<sup>12</sup> With the assumed measurement noise, the performance of the designed Kalman filter is good and yields minimum estimation errors. However, for the real-world applications, the process and measurement noise may need to be tuned further to improve the overall filter performance under model mismatch conditions. In general, the process and measurement noise needs to be accounted at appropriate levels. If a system model has too much noise, then it will be difficult to estimate its states and with less measurement noise the state estimator might be more susceptible to modeling errors.<sup>30</sup> The implementation of the EKF algorithm involves the following steps:

1. Compute the  $F_k$  and  $L_k$  matrices

$$F_k = \left. \frac{\partial f_{k-1}}{\partial x} \right|_{x_{k-1}, u_{k-1}} \quad (12)$$

$$L_k = \left. \frac{\partial f_{k-1}}{\partial w} \right|_{x_{k-1}, u_{k-1}} \quad (13)$$

2. Predict the state and error covariance

$$x_k^- = f_{k-1} (x_{k-1}^+, u_{k-1}, 0) \quad (14)$$

$$P_k^- = F_{k-1} P_{k-1}^+ F_{k-1}^T + L_{k-1} Q_{k-1} L_{k-1}^T \quad (15)$$

3. Compute the matrices of  $H_k$  and  $M_k$

$$H_k = \left. \frac{\partial h_k}{\partial x} \right|_{x_k^-} \quad (16)$$

$$M_k = \left. \frac{\partial h_k}{\partial v} \right|_{x_k^-} \quad (17)$$

4. Compute the optimal Kalman gain

$$K_k = P_k^- H_k^T (H_k P_k^- H_k^T + M_k R_k^- M_k^T)^{-1} \quad (18)$$

5. Compute the state estimate and error covariance

$$x_k^+ = x_k^- + K_k (y_k - h_k(x_k^-, 0)) \quad (19)$$

$$P_k^+ = (I - K_k H_k) P_k^- (I - K_k H_k)^T + K_k R_k K_k^T \quad (20)$$

where the superscript “−” denotes the estimate of an value before the measurement at time  $k$  and the superscript “+” denotes the estimate of the same value after the measurement at time  $k$ .

Steps 1–5 are followed at each time step and the optimal gain matrix and state estimates are calculated. The temperature states for the discretized  $5 \times 5$  zone reduced order MPF model are defined as follows

$$x_k = \begin{Bmatrix} T_{2,k} \\ T_{3,k} \\ T_{4,k} \\ T_{5,k} \\ T_{7,k} \\ \cdot \\ \cdot \\ T_{25,k} \end{Bmatrix} \quad (21)$$

[Figure 7](#) shows the schematic of the CPF temperature states for the  $5 \times 5$  zone CPF state estimator. The input temperatures for the CPF state estimator are  $T_1, T_6, T_{11}, T_{16}$ , and  $T_{21}$ , and they are calculated from the DOC outlet temperature  $T_{in,4}$  using the thermal boundary layer equations explained in Mahadevan et al.<sup>2</sup> The physical temperature sensor was mounted close to  $T_{out,20}$  location shown in [Figure 7](#) and was used to improve the temperature estimates ( $x_k^+$ ) as shown in [equation \(19\)](#). The function  $f$  for each temperature state is determined from the discretized system model [equation \(8\)](#) at various locations of the axial and radial temperature states ( $T_1$  to  $T_{25}$ ).

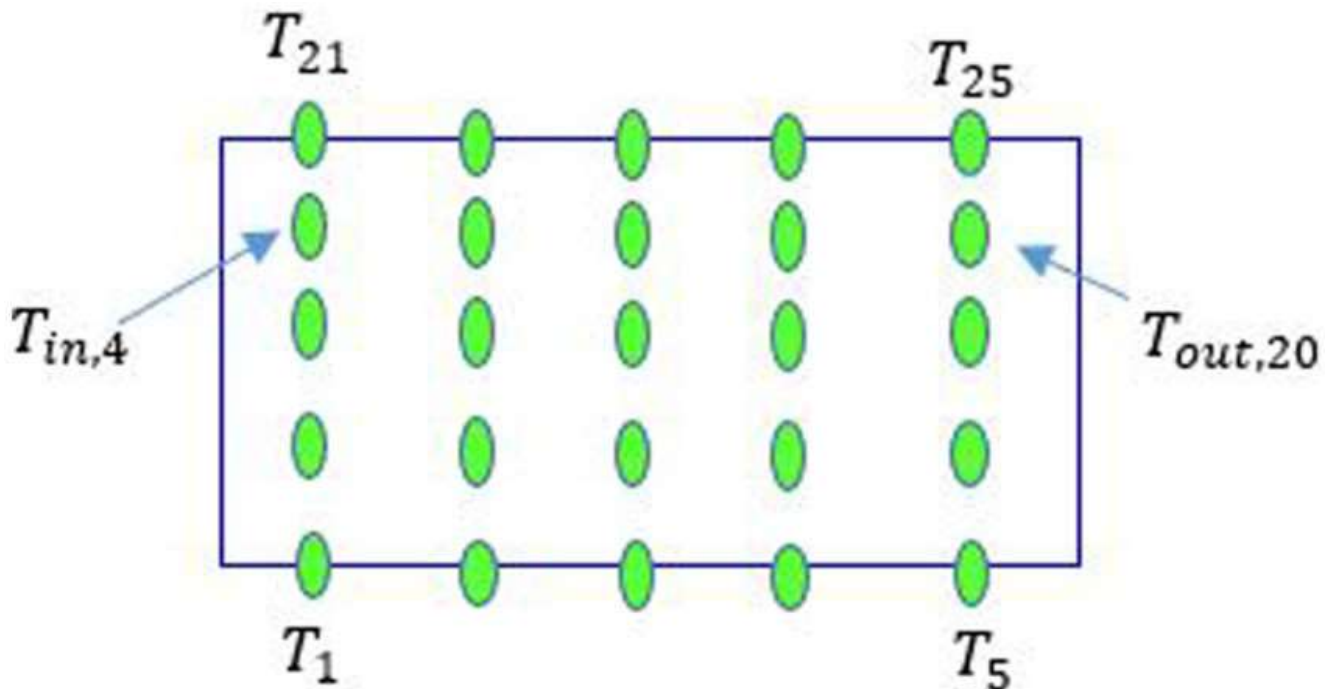


**Figure 7.** Schematic of temperature states of the CPF estimator.

The temperature states ( $T_1$  to  $T_{25}$ ) from the EKF were used for determining the oxidation of PM cake and wall at each axial and radial location of the CPF. From the oxidation rates of PM cake and wall, the PM mass retained and PM mass retained distribution within the CPF was estimated. The detailed estimator equations for the PM mass retained distribution are shown in [Appendix B](#) of Supplementary Material.

LKF for pressure drop estimation

The temperature and PM mass distribution can be accurately estimated using the temperature state estimates. However, at constant flow and temperature conditions, the pressure drop across the filter is governed by the following parameters:

- PM flow rate (PM concentration and volumetric flow rate);
- Thickness of the PM cake layer (PM mass retained);
- PM within the pores of the substrate wall resulting from wall filtering;
- PM cake oxidation rate (temperature,  $\text{NO}_2$ , and  $\text{O}_2$  concentrations);
- PM wall oxidation rate (temperature,  $\text{NO}_2$ , and  $\text{O}_2$  concentrations);
- Permeability of wall (clean wall, packing density, partial oxidation of PM in the wall, slip flow, etc.);
- Permeability of cake (initial, damage values, damage recovery, slip flow, etc. as explained in reference [3].).

Based on the fact that the above parameters affect the pressure drop, it is evident that the temperature estimates and subsequent PM oxidation alone are not good enough to accurately predict the pressure drop. Hence, the LKF is necessary such that the measured total pressure drop from the ECU sensor can be used to predict unknown components of the pressure drop measurement such as cake pressure drop.

The state space representation of a linear model with state  $x_k$  and noises  $w_k$  and  $v_k$  can be represented by

$$x_k = Ax_{k-1} + w_{k-1} \quad (22)$$

$$z_k = H_k x_{k-1} + v_k \quad (23)$$

The implementation algorithm for the LKF is given as follows

Predict the state and error covariance

$$x_k^- = Ax_{k-1}^+ \quad (24)$$

$$P_k^- = AP_{k-1}^+ A^T + Q_{k-1} \quad (25)$$

2. Compute optimal Kalman gain

$$K_k = P_k^- H_k^T (H_k P_k^- H_k^T + R_k)^{-1} \quad (26)$$

3. Compute the state estimate and error covariance

$$x_k^+ = x_k^- + K_k (z_k - H_k x_k^-) \quad (27)$$

$$P_k^+ = P_k^- - K_k H_k P_k^- \quad (28)$$

The state  $x_k$  is estimated total pressure drop and the output  $z_k$  is the measured total pressure drop. The process noise ( $w_k$ ) is assumed to be equal to zero and the covariance for the measurement ( $R_k$ ) is calculated assuming standard Gaussian distribution with deviation of 0.5 kPa for the measurement noise ( $v_k$ ). The other components of pressure drop such as cake and wall pressure drops and total channel pressure drop are determined as follows.

The estimated cake pressure drop is given as follows

$$(\Delta P_{\text{cake}})_k = (\Delta P_{\text{total}} - \Delta P_{\text{wall}} - \Delta P_{\text{channel}})_k \quad (29)$$

The detailed estimator equations for terms used in [equation \(29\)](#) is shown in [Appendix B](#) of Supplementary Material.

The CPF state estimator estimates the temperature states at axial and radial locations of the filter. The temperature state estimates are used to predict PM filtration, PM oxidation, and pressure drop of the CPF using the model equations developed in Mahadevan et al.<sup>2,3</sup> Furthermore, LKF within the CPF state estimator uses the measured  $\Delta P$  sensor signal ( $\Delta P_{\text{total}}$  in [equation \(29\)](#)) values to estimate the unknown states of the pressure drop such as cake pressure drop using [equation \(9\)](#). The CPF estimator temperature ( $T_{\text{in},4}$ ) and the CPF inlet concentrations ( $\text{NO}_2$ ,  $\text{O}_2$ , and  $\text{C}_3\text{H}_6$ ) are determined from the DOC state estimator developed in Surenahalli et al.<sup>11</sup> The next section explains the integration of DOC state estimator with the CPF state estimator.

## Results

The DOC-CPF state estimator is simulated for one of the active regeneration experiments (AR-B10-1) and the results are compared with the  $10 \times 10$  high-fidelity model and experimental data. The DOC-CPF state estimator uses the reduced order model explained in section “Reduced order model development,” to predict the temperature states of the current time ([equation \(19\)](#)). Furthermore, the temperature estimates are improved by the EKF algorithm explained in section “Development of Kalman filter–based CPF state estimator.” The inputs to the DOC-CPF estimators were sampled at 1 Hz. The discrete time step solver with 1-s time step was used to run the DOC-CPF state estimator. With the fixed step discrete solver and the model time step of 1 s, the DOC-CPF state estimator takes 15.2% of total real time or about 6.5 times faster than the real time using the laptop computer with the specifications of 12 GB RAM, 64 bit and Intel core i7 processor.

The active regeneration experimental (AR-B10-1) data were used for the validation of DOC-CPF state estimator. The selection of AR-B10-1 experiment is because the CPF estimator needs to consider the high filter substrate temperatures in the CPF and short PM oxidation duration as they greatly affect the temperature and PM mass retained distribution of the filter. The CPF estimator used the  $\text{NO}_2$  outlet concentration from the DOC estimator and  $\text{O}_2$

concentration measured at the inlet to the DOC. The DOC state estimator results in comparison with experimental data are presented in [Appendix C](#) of Supplementary Material. The reaction kinetics of the DOC estimator were calibrated to simulate AR-B10-1 experiment and the calibrated kinetics are shown in Table C.1 in [Appendix C](#) of Supplementary Material.

### CPF outlet temperature

[Figure 8](#) shows the comparison of DOC-CPF state estimator outlet gas temperature (Estimated) with the CPF experimental outlet gas temperature measured during the AR-B10-1 experiment. From [Figure 8](#), the estimated outlet gas temperature ( $x_k^+$ ) closely simulated the experimental data using the optimal Kalman gain ( $K_k$ ) and measured sensor data ( $y_k$ ) as shown in [equation \(19\)](#) of section “EKF for temperature distribution estimation.” The optimal Kalman gains are calculated using [equation \(18\)](#) shown in “EKF for temperature distribution estimation.” The Kalman filter algorithm computes the final estimate ( $x_k^+$ ) by calibrating the initial estimate ( $x_k^-$ ) with the prediction error ( $y_k - h_k(x_k^-, 0)$ ) of the measurement using [equation \(19\)](#). In order to accurately account for the prediction error, the accuracy of the system model is critical for the estimator. The reduced order model developed in section “Reduced order model development” showed capability in accurately predicting the temperatures.<sup>17</sup> Hence, the estimated temperature closely follows the measured outlet gas temperature. The CPF estimator closely simulated the sensor feedback which is close to  $T_{20}$  location (exhaust gas temperature sensor with insertion length of 33 mm) as shown in [Figure 7](#).

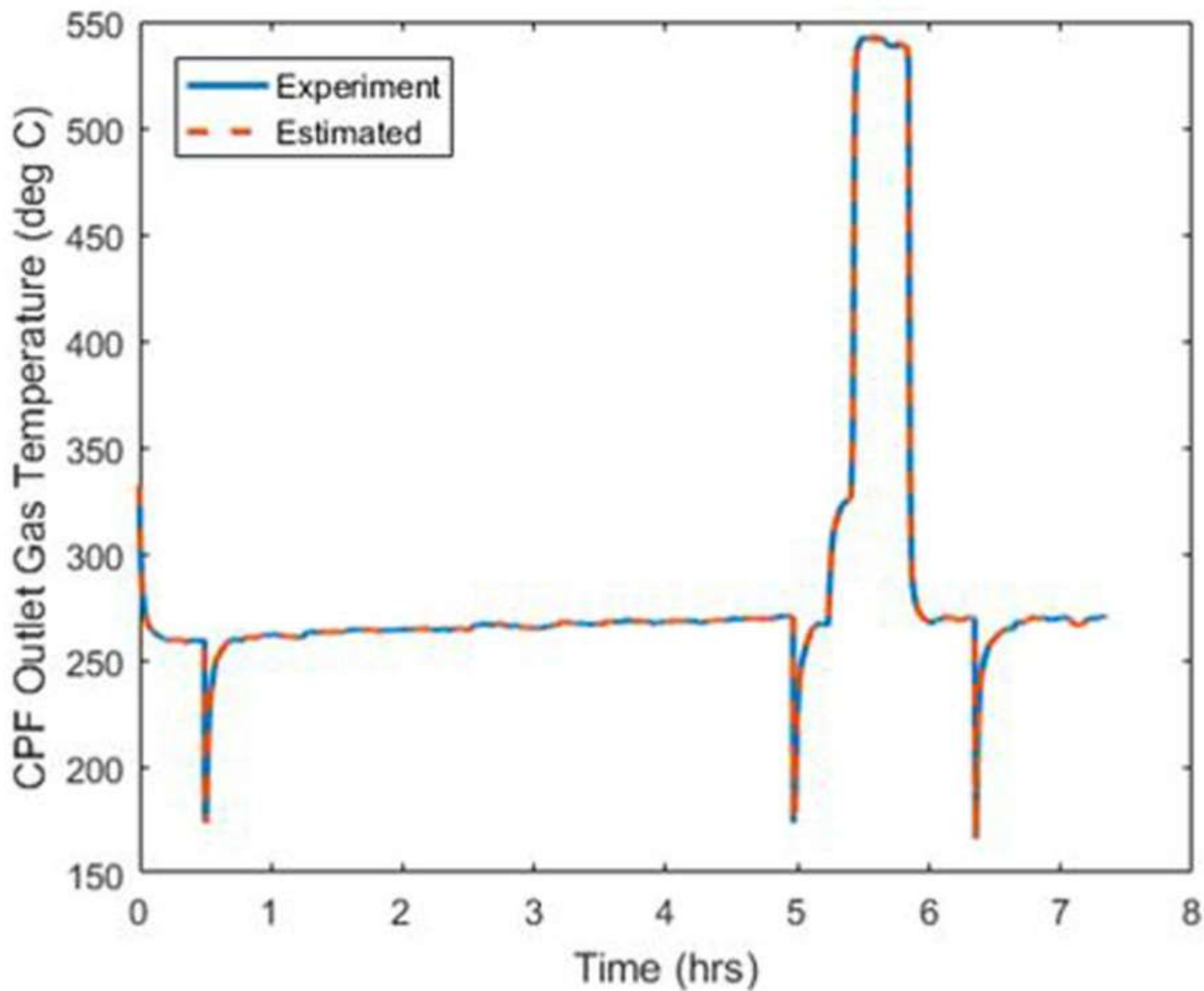


**Figure 8.** Comparison of DOC-CPF estimator outlet gas temperatures along with the measured CPF outlet gas temperature for AR-B10-1 experiment.

#### CPF temperature distribution

[Figure 9](#) shows the comparison of the CPF experimental and DOC-CPF estimator temperature distribution at 5.63 h (15 min after start of fuel dosing). From [Figure 9](#), the DOC-CPF state estimator is able to closely follow the experimental temperature distribution and the maximum absolute temperature difference between the DOC-CPF estimator and the experimental data are less than 5 °C for radiiuses less than 120 mm. The RMS temperature error is  $\cong 32$  °C. In [Figure 9](#), the temperature distribution varies axially as well as radially. The radial variation in temperature distribution is  $\cong 40$  °C and axial variation in temperature is  $\cong 12$  °C. The CPF temperature is maximum close to the outlet (filter length 50 mm) due to the oxidation of PM and HC within the CPF. By knowing the temperatures

at various locations of the CPF, a control action based on good data can be taken for CPF regeneration while accounting for the zonal temperatures within the CPF.

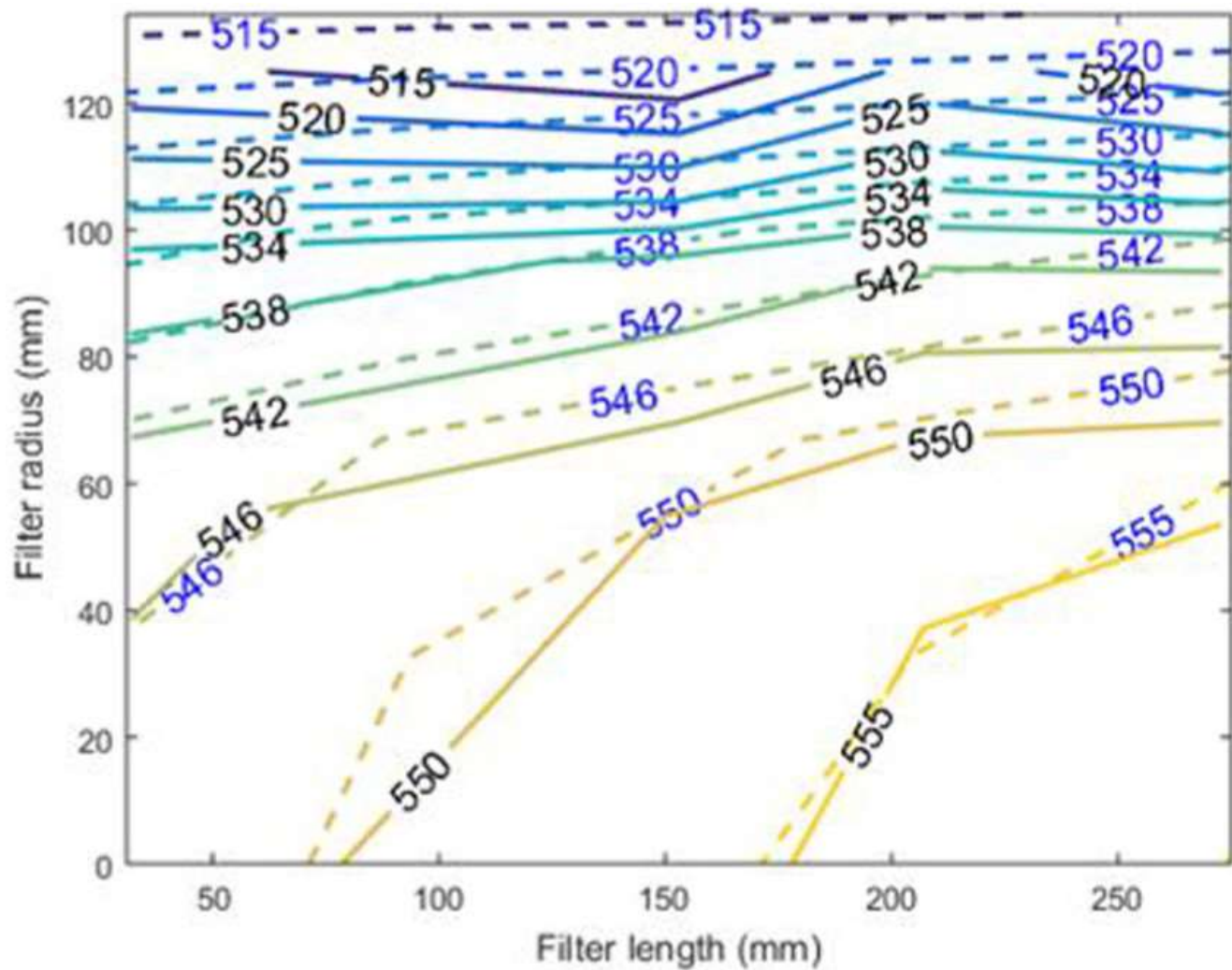


**Figure 9.** Comparison of CPF experimental (solid lines) and DOC-CPF estimator (dashed line) temperature distribution in °C at 5.63 h (15 min after start of fuel dosing).

PM mass retained

[Figure 10\(a\)](#) shows the comparison of the estimated total PM mass retained and experimental data for AR-B10-1 experiment. The estimated total PM mass retained closely agrees with the experimental data and the maximum absolute error is 1.2 g at the end of stage 2 loading (at 4.9 h). [Figure 10\(b\)](#) shows the comparison of cake and wall PM masses for the DOC-CPF state estimator and the high-fidelity CPF model. From [Figure 10\(b\)](#), the nated wall and cake PM closely simulates the high-fidelity model data. The absolute

error between estimator and high-fidelity model is  $\cong 1.6$  g at 5.42 h (at end of AR RU phase) for cake PM and  $\cong 0.6$  g at 5.31 h for wall PM. The estimated wall PM mass at the end of stage 2 loading (4.9 h) is 2.6 g or 6% of total PM mass retained and estimated cake PM mass is 44.3 g or 94% of total PM mass retained. Most of the wall PM is oxidized during PM oxidation and the wall PM mass is reduced to  $\cong 0.3$  g. The PM in the substrate wall affects the pressure drop trends. Using the DOC-CPF estimator in an ECU, the CPF regeneration strategy can also consider PM levels in the substrate wall for optimum regeneration time.

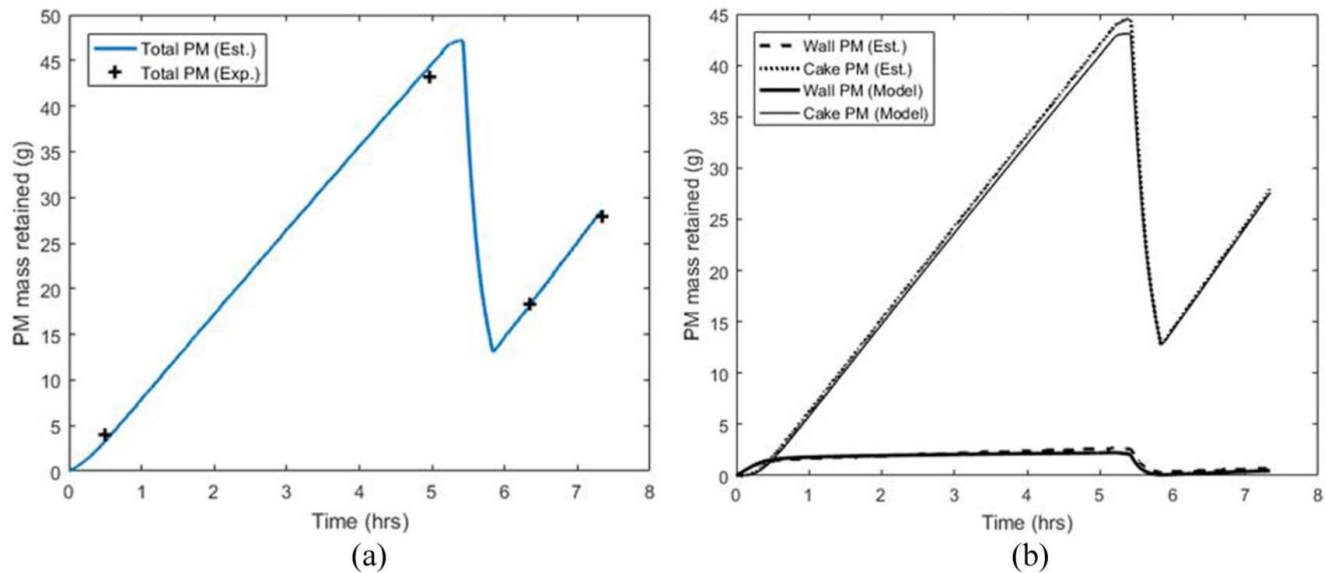


**Figure 10.** Comparison of PM mass retained for AR-B10-1 experiment: (a) estimated total PM mass retained in comparison with experimental data and (b) estimated cake and wall PM masses in comparison with high-fidelity model.

## PM distribution

[Figure 11](#) shows the comparison of PM mass retained distribution in the axial and radial directions at the end of PM oxidation (at 5.82 h) by active regeneration for AR-B10 experiment simulated by the DOC-CPF estimator and the high-fidelity CPF model. In [Figure 11](#), the PM mass retained distribution simulated by the DOC-CPF state estimator agrees closely with the data from the high-fidelity model. The PM mass retained distribution difference is less than 0.1 g/L compared to high-fidelity CPF model for filter radiiuses less than 120 mm. The PM loading distribution simulated by the DOC-CPF state estimator is  $\sim 0.2 - 0.5$  g/L lower than the high-fidelity model at outer radiiuses of the filter (radiiuses  $> 120$  mm). This is mainly because of the lower discretization of the DOC-CPF estimator

compared to the high-fidelity CPF model. The PM mass retained distribution near the center of the filter (radiiuses < 60 mm) and axially >50 mm, the DOC-CPF estimator underestimates the PM mass retained distribution by  $\approx 0.05$  g/L compared to the high-fidelity model. This is also mainly due to the lower discretization of the DOC-CPF estimator compared to the high-fidelity model and causing small differences ( $\leq 2$  °C) in temperature distribution and corresponding changes in PM oxidation and mass distribution in the CPF. In [Figure 11](#), the PM mass retained is minimum at the center of the filter compared to the outer radiiuses. This is mainly due to the lower exhaust gas temperature at the outer radiiuses due to the convective and radiative heat losses to the ambient as shown in [Figure 9](#). By knowing the local PM mass distribution within the filter, the CPF regeneration strategy (time at a given temperature) can be optimized to minimize excess PM loading thereby reducing the possibility of future localized exotherms due to PM buildup. This improved PM mass retained distribution data could improve the durability of the CPF.

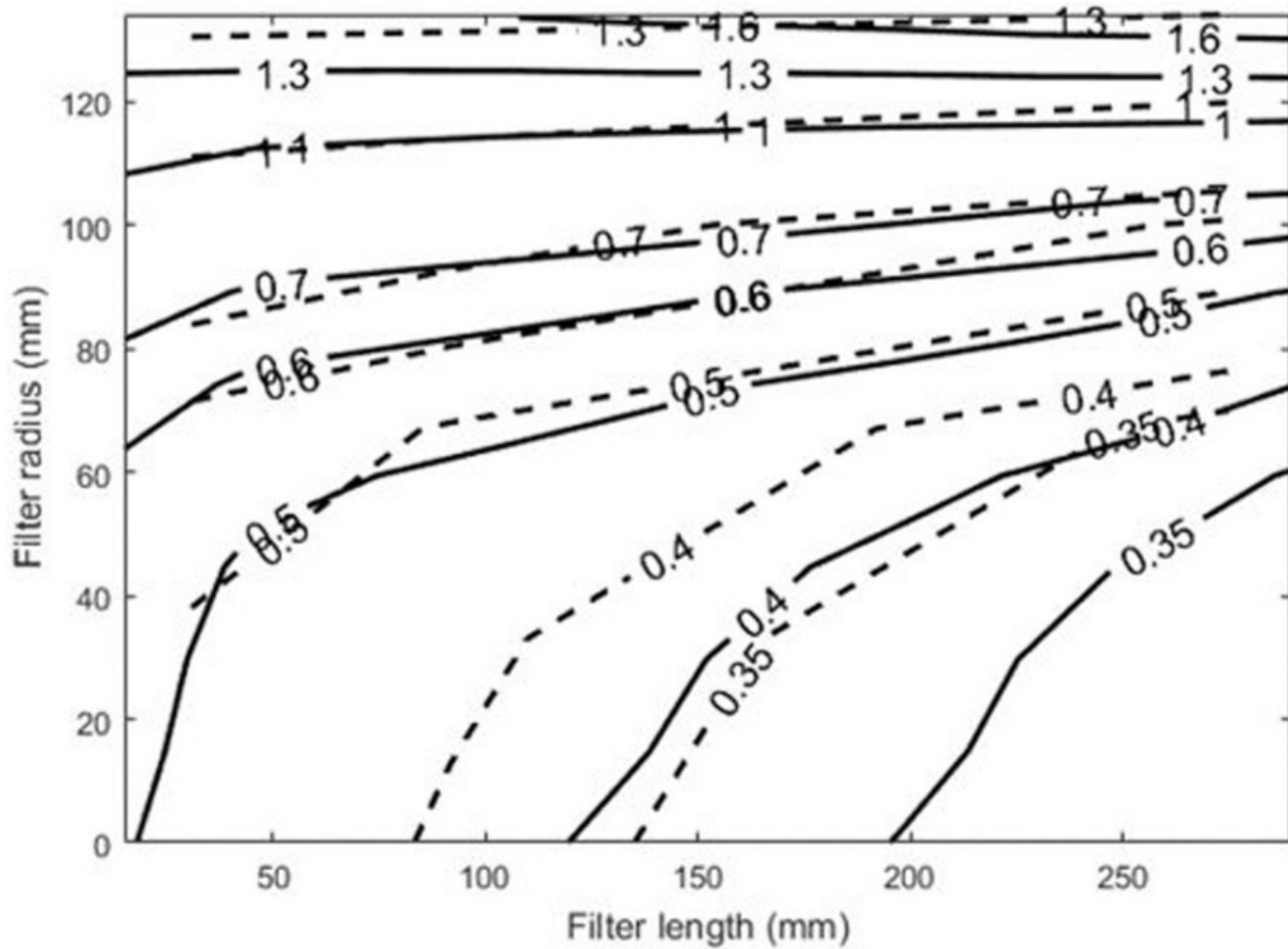


**Figure 11.** Comparison of high-fidelity model (solid lines) and closed loop DOC-CPF PM mass retained distribution in g/L at 5.82 h (end of PM oxidation by active regeneration) for AR-B10-1 experiment.

Pressure drop

[Figures 12](#) shows the comparison of the total pressure drop across the CPF and its components for AR-B10-1 experiment simulated by the high-fidelity model and the DOC-CPF estimator. For the calibration of the high-fidelity model, the experimental data from 18 experiments (6 passive oxidation and 12 active regeneration experiments) with three different fuels (ULSD, B10, and B20) were used. The objective of the calibration procedure was to determine single set of calibration parameters for the high-fidelity model simulation. With the single set of calibration parameters, the simulated RMS pressure drop error of 18 experiments compared to the experimental data was within 0.2 kPa.<sup>17</sup> The detailed model development, calibration, and results are available in Mahadevan.<sup>17</sup>

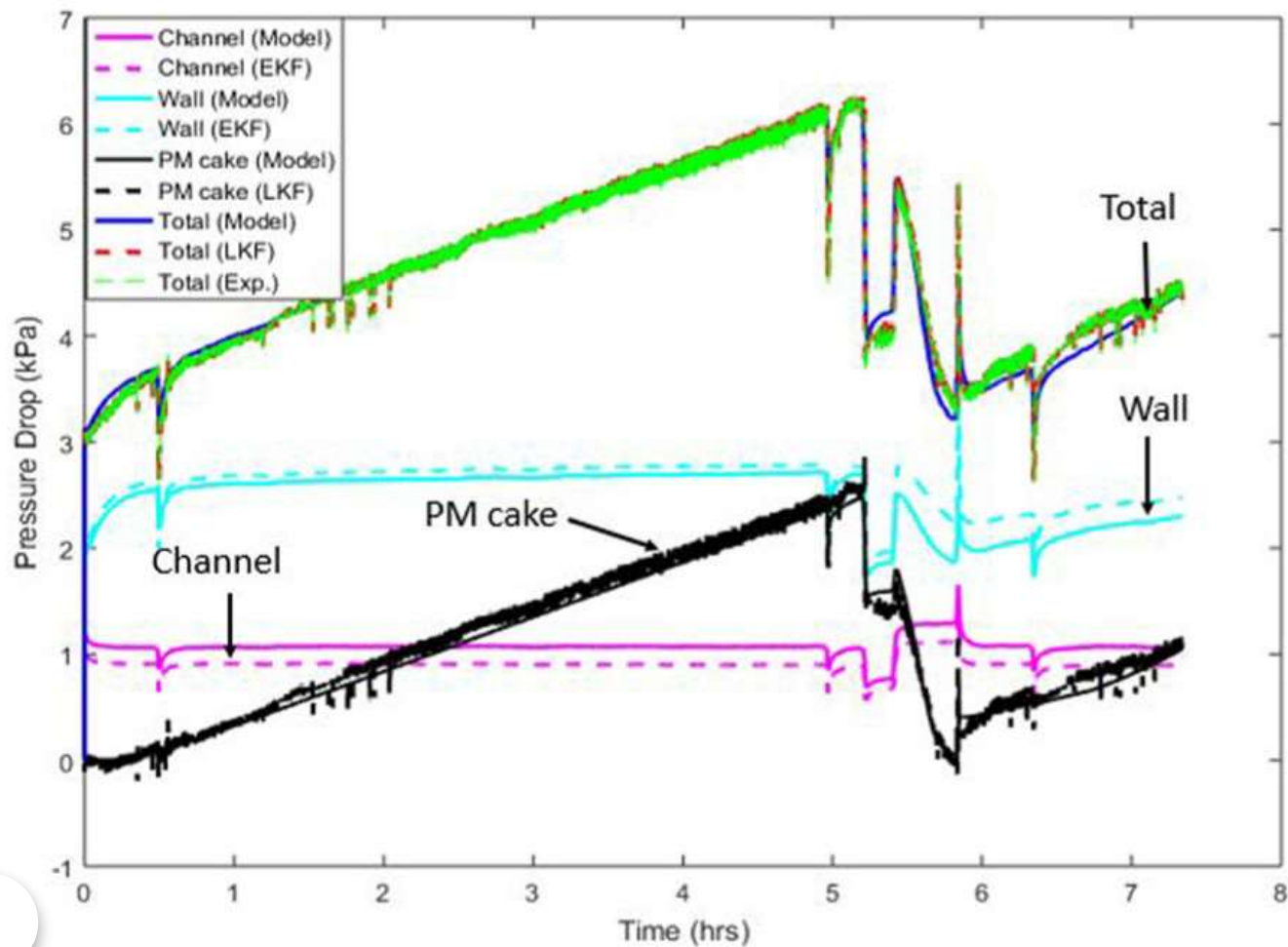


**Figure 12.** Comparison of experimental total pressure drop across CPF and its components (i.e. channel, wall, and cake) for AR-B10-1 experiment using high-fidelity model and DOC-CPF estimator for pressure drop.

The non-linear change in pressure drop at the start of the test in Figure 12, is the “deep bed” filtration period where the substrate pores fill with PM in the wall and it lasts about 30 minutes. These data are used for the high-fidelity model calibration. Comparing high-fidelity model-simulated total pressure drop with experimental data in [Figure 12](#), the simulated pressure drop values are in good agreement with the experimental data with a maximum absolute difference of  $\cong 0.3$  kPa during AR ramp phase of the experiment (5.3 h). The total pressure drop estimated by the DOC-CPF estimator closely follows the experimental data. The LKF estimated total pressure drop agrees closely ( $\cong 0.1$  kPa) with the measured pressure drop using the optimal Kalman gain and the  $\Delta P$  feedback from the pressure sensor as shown in [equation \(27\)](#). Comparing the total pressure drop estimated by LKF estimator with the total pressure drop estimated by high-fidelity model in [Figure 12](#), the LKF estimator closely agrees with the experimental data than the high-fidelity model. The LKF estimator used the reduced order model developed from the high-fidelity model. The reduced order model also has pressure drop errors up to  $\cong 0.4$  kPa.<sup>17</sup> However, the LKF estimator data closely agrees better with the experimental data than the high-fidelity model data. This is mainly because the LKF estimator calibrated the prediction error ( $z_k - H_k x_k^-$ ) of the system model with the measurement signal using [equation \(27\)](#). Hence, the LKF estimator was able to closely follow the experimental data at every time step. The cake pressure drop was estimated using the LKF estimator using the model [equation \(9\)](#) and the estimated cake pressure drop error is within  $\cong 0.2$  kPa compared to high-fidelity model. The channel and wall pressure drop values are calculated using the temperature and PM mass loading estimates of the EKF estimator. The EKF-based channel and wall pressure drop data are within  $\cong 0.2$  kPa compared to the high-fidelity model.

[Figure 13](#) shows the estimated cake pressure drop for various cake PM loading during the AR-B10-1 experiment. Symbols S1, S2, S3, and S4 show the various stages of the AR-B10-1 experiment. From [Figure 13](#), three distinct regions of CPF operation can be determined. (1) During stage 1 and 2 loading (S1 and S2), the cake pressure drop increases linearly as a function of cake PM loading within the filter. (2) During PM oxidation (between two thick solid arrows) by active regeneration, the cake pressure drop reduces as the PM cake oxidizes

through thermal ( $O_2$ ) and  $NO_2$ -assisted PM oxidation reactions. The pressure drop during PM cake oxidation at a given cake PM loading is lower than the pressure drop during stage 1 and 2 loading due to the different flow rate during PM oxidation causing reduced flow resistance as well as the increased permeability of the PM cake layer due to the damage in the PM cake as explained in Mahadevan et al.<sup>3</sup> The start of PM cake damage during PM oxidation by active regeneration is shown as the dashed red arrow in [Figure 13](#). The sudden reduction in cake pressure drop during the AR ramp phase of the experiment (marked as AR Ramp in [Figure 13](#)) is due to the change in flow conditions causing the reduced flow resistance in the PM cake layer. The wall pressure drop reduces significantly during PM oxidation by active regeneration and approaches the clean wall pressure drop because of oxidation of PM within the substrate wall as shown in [Figure 10\(b\)](#). (3) During post-loading (stage 3 and 4 loading), the cake pressure drop increases proportional to the PM cake loading; however, the cake pressure drop at a given PM cake mass is lower than the cake pressure drop estimated during stage 1 and stage 2 loading. This is mainly because of the presence of the damaged cake layer and lower mass in the wall and then to the earlier PM oxidation by active regeneration and because the cake filters the PM and letting only small masses into the wall.

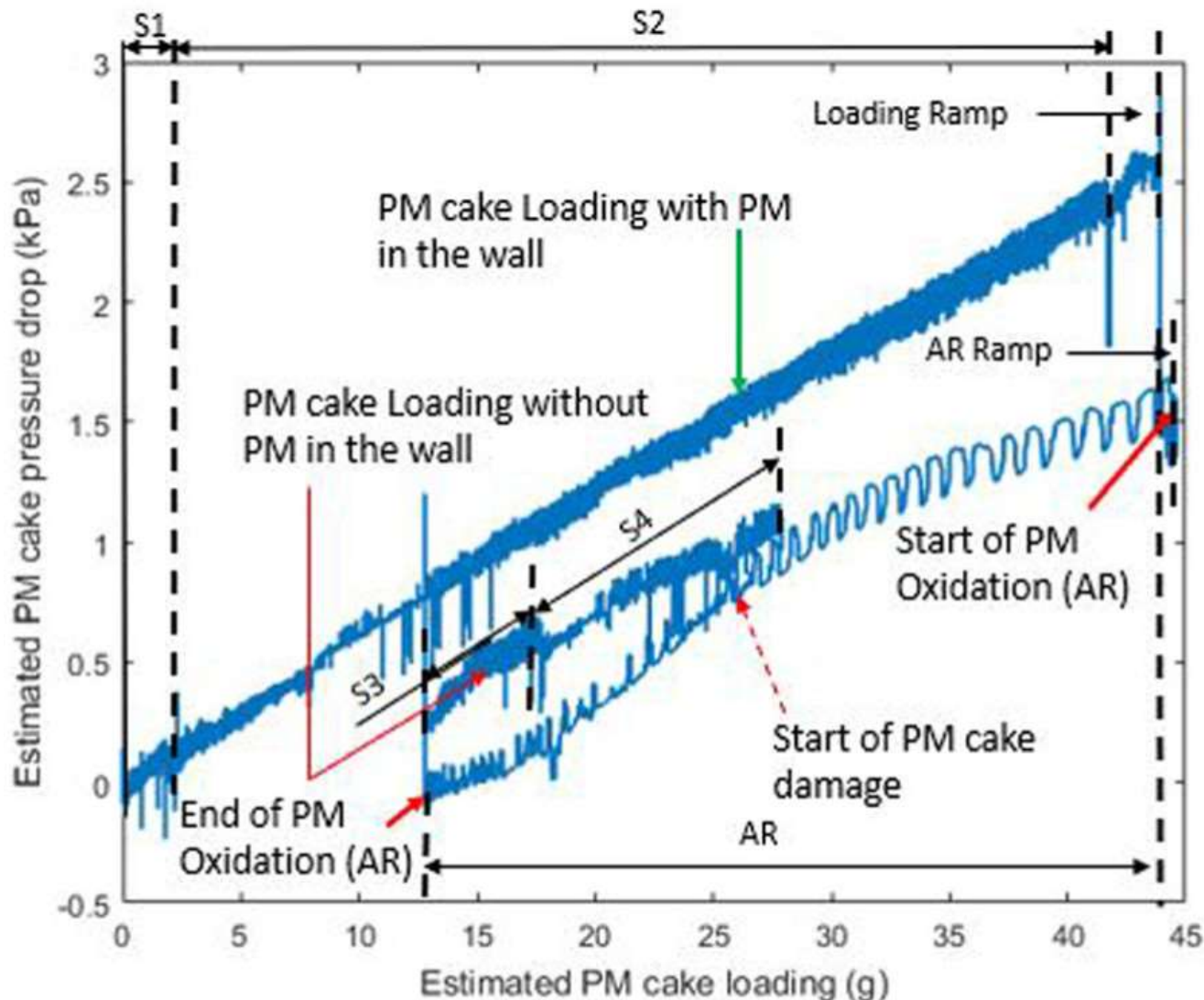


**Figure 13.** PM cake loading versus PM cake pressure drop estimated using linear Kalman estimator during AR-B10-1 experiment. S1, S2, AR, S3, and S4 show stage 1, stage 2, active regeneration, stage 3, and stage 4 phases of the experiment as a function of time, respectively.

By comparing cake pressure drop estimates along with the wall and channel pressure drop estimates, appropriate control actions can be taken in the event of failure of sensors, failure of components, or excess PM loading of the CPF. For example, in the event of cracked substrate wall, the overall pressure drop measured by the  $\Delta P$  pressure sensor will be lower causing negative estimated cake pressure which is an indication of failure of a component and can be determined by the pressure drop estimator. Without a pressure drop estimator, it will be difficult to diagnose the problem, because the measured pressure drop will still be

non-zero and within upper and lower bounds of the typical CPF operational checks of the ECU; thus, this crack would not be diagnosed by conventional ECU OBD strategies.

From the analysis results in section “Results,” it is evident that the designed DOC-CPF state estimator shows the capability to predict temperature and PM mass retained distribution and pressure drop of the CPF at various operating conditions. The DOC-CPF state estimator used the engine outlet exhaust gas temperature and NO<sub>x</sub>, HC, and O<sub>2</sub> concentrations from the ECU sensors or maps to estimate the temperature and PM distribution and PM mass retained and the pressure drop components of the CPF. With the EKF for temperature estimation and LKF for pressure drop estimation, the outlet gas temperature and  $\Delta P$  across the CPF were closely simulated with the measured sensor signals. The RMS error in estimated temperature distribution by the DOC-CPF state estimator is within 3.2 °C and the absolute error for PM mass retained distribution was within 0.7 g of the experimental data at the end of stage 4 loading. The estimated cake pressure drop was within 0.1 kPa and the channel and wall pressure drop values are within 0.2 kPa compared to the high-fidelity model.

## Summary and conclusion

A reduced order MPF model was developed to reduce the computational time and the complexity of the CPF model for use in an ECU-based application through using a CPF state estimator. A parametric study was carried out to determine the number of zones for the reduced order MPF model. It was found that the 5 × 5 zone model was sufficient to provide the required accuracy while having required computational speed for real-time operation. Further model reduction assumptions were evaluated to improve the computational speed without significantly affecting the accuracy of the model prediction.

A CPF state estimator was developed to predict unknown states of the CPF such as temperature distribution, PM mass retained, PM mass retained distribution, and pressure drop components across the CPF. An EKF state estimator was developed to predict unknown temperature states. In addition, a LKF estimator was developed to predict unknown components of the pressure drop such as the cake pressure drop. The DOC state estimator developed by Surenahalli et al.<sup>11</sup> was integrated with the CPF state estimator to provide inlet conditions of DOC outlet temperature, NO<sub>2</sub>, and HC concentrations to the CPF. The integrated DOC-CPF model was validated on an active regeneration test condition. The DOC-

CPF state estimator was shown to have the capability to predict 2D temperature distribution, PM mass retained, PM distribution, and the pressure drop components across the CPF.

In practical systems, the temperature and PM mass distributions are also affected by the 3D inlet flow and temperature distributions. Ranalli et al.<sup>31</sup> showed that the inlet pipe geometries affect the velocity and flow distribution within the pipe. The flow distribution could affect the PM loading, oxidation, and pressure drop distribution within the CPF. The reduced order model and CPF estimator presented in this research assumes the uniform flow and species distribution at the inlet of the CPF. For 3D non-uniform flow and species concentration distribution, the reduced order 2D model and state estimator developed in this work needs to be expanded by discretizing the CPF in the circumferential direction and solving a separate 2D state estimator at each circumferentially discretized location. With the fixed step discrete solver and the model time step of 1 s, the real-time factor for the DOC-CPF state estimator is 0.152 (15.2% of real time or  $\approx$ 6.5 times faster than the real time) using the Laptop computer with the specifications of 12 GB RAM, 64 bit and Intel core i7 processor. For 3D CPF state estimation, the real-time factor could be higher than 1 depending on the number of circumferential discretization which increases the computational time, cost, and complexity. However, by optimizing the number of zones of a 3D CPF state estimator along with additional model reduction assumptions on flow and concentration distribution, a real-time 3D CPF estimation may be possible in future vehicles with increased ECU processing capability or a standalone vehicle ECU for CPF controls.

In order to apply the Kalman filter-based approach for the simulation of other particulate filters with very different microstructure such as gasoline particulate filter (GPF) with inhomogeneous porosity and pore size distribution in Gong et al.,<sup>32</sup> the filtration model within the reduced order model equations have to be modified to account for the varying porosity and pore size distribution within each zone of the multi-zone reduced order model presented in this work. In the reduced order MPF model, the substrate wall within each zone is discretized into  $n$  number of slabs. At each slab, the porosity of the substrate wall is evolved based on the PM mass deposition on a series of spherical collectors considering the Brownian diffusion and interception filtration mechanisms.<sup>17</sup> With the inhomogeneous porosity and pore size distribution of the filters, the initial porosity of the each slab of the substrate wall will have to be modified along with the varying diameters of the spherical collectors as explained in Gong et al.<sup>32</sup> By accounting for the varying porosity and pore size distribution (i.e. diameter of the spherical collector) for each slab, the filtration efficiency, wall permeability, and wall pressure drop can be estimated at each zone using the reduced order

MPF model classical filtration equations in Mahadevan<sup>17</sup> and EKF equations presented in this research.

In the real-world production systems, there could be an uncertainty in the thermal and physical properties of the selected configuration of the CPF due to the manufacturing process variations (e.g. part to part variability), uncertainties in the real and virtual sensor inputs (such as exhaust mass flow, temperature, inlet species concentrations, and  $\Delta P$ ) used in the CPF estimator. Hence, the sensitivity study for the uncertainty in thermal and physical properties along with the uncertainty in sensor inputs to the CPF estimator is important for the development of a robust CPF controller that is planned for future studies.

The specific conclusions are as follows:

- From the discretization study, a  $5 \times 5$  zone CPF model was found to be four times faster than the baseline  $10 \times 10$  model with RMS temperature prediction error of  $3.5^{\circ}\text{C}$ , absolute PM loading difference of 1.6 g at the end of stage 4 loading and absolute pressure drop difference of 0.2 kPa at the end of stage 4 loading, compared to the experimental data.
- With the DOC-CPF estimator, the PM loading error is within 0.7 g at the end of stage 4 loading, the RMS temperature prediction error during PM oxidation by active regeneration is  $3.2^{\circ}\text{C}$ . In addition, the pressure drop estimates closely ( $<0.1$  kPa) agree with the experimental data using the linear pressure drop Kalman estimator and the estimated cake pressure drop error is within 0.2 kPa compared to the high-fidelity model. The estimated channel and wall pressure drop data are within 0.2 kPa compared to the high-fidelity model.
- The  $\Delta P$  sensor-based CPF diagnostics is incapable of detecting component failures such as cracked wall, whereas LKF-based  $\Delta P$  estimator shows improved diagnostics capability that can differentiate pressure drop between various components of the CPF pressure drop such as PM cake, wall, and channel pressure drops.

## Acknowledgments

The authors would like to thank Kenneth Shiel and James Pidgeon of Michigan Technological University for collecting the temperature distribution data presented in this paper. Special thanks go to Venkata Chundru for developing the species solver and improved temperature

solver used in high-fidelity CPF model and Dr Gordan Parker for guidance on developing the architecture of the high-fidelity model MATLAB code.

## Declaration of conflicting interests

The author(s) declared no potential conflicts of interest with respect to the research, authorship, and/or publication of this article.

## Funding

The author(s) disclosed receipt of the following financial support for the research, authorship, and/or publication of this article: The experimental data presented in this paper is based upon research work supported by a grant from the United States Department of Energy Award Number DE-EE0000204.

## Appendix 1

### Notation

$a^*$  effective width of an inlet channel loaded with PM (m)

$A$  width of the clean outlet channel (m)

$A_{O_2}$  pre-exponential for thermal ( $O_2$ ) PM oxidation (m/K/s)

$A_{NO_2}$  pre-exponential for  $NO_2$ -assisted PM oxidation (m/K/s)

$c_f$  specific heat of filter material (J/kg/K)

$c_s$  specific heat of PM cake (J/kg/K)

$E_i$  activation energy (kJ/g/mol)

$F$  friction factor in the inlet and outlet channel of the particulate filter (–)

$k$  time step (s)

$k_{cakei,j}$  PM cake permeability at each zone ( $m^2$ )

$k_{NO_2i,j}$  rate constant for  $NO_2$ -assisted PM oxidation at each zone (m/s)

$k_{O_2i,j}$  rate constant for  $O_2$ -assisted PM oxidation at each zone (m/s)

$k_{walli,j}$  substrate wall permeability at each zone ( $m^2$ )

$K$  optimal Kalman gain matrix

$m_{c,i,j}$  PM mass in the PM cake layer at each zone (kg)

$m_{w,i,j}$  PM mass in the substrate wall at each zone (kg)

$n$  slab number index of the substrate wall at each zone (–)

$n_{\max}$  number of the slabs in the substrate wall at each zone (–)

$P_k^-$  error covariance matrix of previous time step

$P_1|_{i,j}$  absolute pressure at the inlet channel of each zone (kPa)

$P_1|_{i,s_1}$  inlet channel pressure for stream line index  $s_1$  (kPa)

$P_2|_{i,j}$  absolute pressure at the outlet channel of each zone (kPa)

PM mass distributio  $n_{i,j}$  PM mass distribution at each zone (g/L)

PM retaine  $d_{i,j}$  PM mass retained at each zone (kg)

$\dot{Q}_{\text{cond,axial}}$  axial conduction heat transfer rate (W)

$\dot{Q}_{\text{conv}}$  convection heat transfer rate between channels gases and filter wall (W)

$\dot{Q}_{\text{cond,radial}}$  radial conduction heat transfer rate (W)

$\dot{Q}_{\text{reac,HC}}$  energy released rate during oxidation of HC in the inlet gas (W)

$\dot{Q}_{\text{reac,PM}}$  energy released during oxidation of PM (W)

$R_k$  covariance matrix for the state estimator (–)

$R_u$  universal gas constant (J/mol/K)

$s$  streamline index (–)

$s_{\max}$  maximum number of stream lines (–)

$s_p$  specific surface area of PM ( $5.5 \times 10^7$ ) (/m)

$t$  time (s)

$T_{\text{amb}}$  ambient temperature (K)

$T_{\text{exit}}$  filter exit gas temperature (K)

$Tf_{i,j}$  temperature of combined filter and PM cake at each zone (K)

$T_{\text{in}}$  CPF inlet temperature (K)

$T_{\text{in},4}$  CPF inlet temperature to state estimator at location 4 (K)

$T_{n,k}$  temperature estimate from CPF state estimator at location  $n$  for current time step (K)

$T_{\text{out},20}$  CPF outlet temperature measured by a sensor at location 20 (K)

$u_k$  state estimator inputs matrix

$l_{i,j}$  average velocity through wall layer in each radial zone (m/s)

$v_{1i,j}$  inlet channel velocity (m/s)

$v_{2i,j}$  outlet channel velocity (m/s)

$v_{si,j}$  velocity of gas through the PM cake at each zone (m/s)

$v_{wi,j}$  velocity of gas through the substrate wall at each zone (m/s)

$v_k$  state estimator observation noise matrix

$VF_i$  volume fraction of exhaust gas flow at each radial section (-)

$V_{f_{i,j}}$  substrate volume in each zone ( $\text{m}^3$ )

$V_{s_{i,j}}$  PM cake volume in each zone ( $\text{m}^3$ )

$w_k$  state estimator process noise matrix

$W_C$  molecular mass of carbon (kg/kmol)

$W_{\text{O}_2}$  molecular mass of oxygen (kg/kmol)

$W_{\text{NO}_2}$  molecular mass of nitrogen dioxide (kg/kmol)

$w_{pi,j}$  PM cake thickness at each zone (m)

$w_s$  substrate wall thickness (m)

$x_k$  states in the CPF state estimator

$\bar{x}_k$  state estimate before the measurement

$x_k^+$  state estimate after the measurement

$y_k$  state estimator output matrix for temperature estimator

$Y_{i,j\text{NO}_2}$  mass fraction of inlet  $\text{NO}_2$  at each zone (-)

$Y_{i,j\text{O}_2}$  mass fraction of inlet  $\text{O}_2$  at each zone (-)

$z_k$  state estimator output matrix for pressure drop estimator

### Subscripts and superscripts

$i$  radial direction

$j$  axial direction

$k$  time step

$n$  substrate wall slab number

$s$  flow stream line index

### Greek variables

$\alpha_{\text{O}_2}$   $\text{NO}_2$  oxidation partial factor (-)

$\alpha_{O_2}$  O<sub>2</sub> oxidation partial factor (–)

$\Delta m c_{i,j}$  change in PM cake mass due to oxidation at each zone (kg)

$\Delta m w_{i,j}$  change in wall PM mass due to oxidation at each zone (kg)

$\Delta L$  effective zone length (m)

$\Delta P$  pressure drop

$\Delta P_{\text{cake}}$  total PM cake pressure drop of the CPF (kPa)

$\Delta P_{\text{cake model}}_{i,j}$  model-simulated PM cake pressure drop at each zone (kPa)

$\Delta P_{\text{channel}}$  total channel pressure drop (kPa)

$\Delta P_{\text{CPF}}$  volume weighted pressure drop of the CPF (kPa)

$\Delta P_{\text{CPF}_i}$  total pressure drop of the CPF at each radial section of the CPF (kPa)

$\Delta P_{\text{exp}}$  total pressure drop across CPF measured during experiment (kPa)

$\Delta P_{\text{est.cake}}$  estimated total PM cake pressure drop across CPF (kPa)

$\Delta P_{\text{total}}$  total pressure drop of the CPF (kPa)

$\Delta P_{\text{total model}}$  model simulated volume averaged total pressure drop of the CPF (kPa)

$\Delta P_{\text{wall}}$  total volume averaged wall pressure of the CPF (kPa)

$\Delta P_{\text{wall}}_{i,j}$  wall pressure drop at each zone (kPa)

$\Delta t$  solver time step (s)

$\Delta x$  discretization length in axial direction (m)

$\eta_{\text{cake}}_{i,j}$  PM cake layer efficiency at each zone (–)

$\eta_{\text{total}}_{i,j}$  total filtration efficiency at each zone (–)

$\eta_{\text{wall}}_{i,j \text{ slab } n}$  wall filtration efficiency at each slab in the zone (–)

$\mu_{i,j}$  dynamic viscosity of exhaust gas at each zone (N s/m<sup>2</sup>)

$\rho_{i,j}$  exhaust gas density at each zone (kg/m<sup>3</sup>)

$\rho_f$  filter substrate density (kg/m<sup>3</sup>)

$\rho_s$  PM cake density (kg/m<sup>3</sup>)

## References

- Rose D, Boger T. Different approaches to soot estimation as key requirement for CPF applications. SAE technical paper 2009-01-1262, 2009.

+ Show References

[Google Scholar](#)

---

2. Mahadevan BS, Johnson JH, Shahbakhti M. Development of a catalyzed diesel particulate filter multi-zone model for simulation of axial and radial substrate temperature and particulate matter distribution. *J Emiss Control Sci Technol* 2015; 1: 183–202.

[+ Show References](#)[Crossref](#)[Google Scholar](#)

---

3. Mahadevan BS, Johnson JH, Shahbakhti M. Predicting pressure drop, temperature, and particulate matter distribution of a catalyzed diesel particulate filter using a multi-zone model including cake permeability. *J Emiss Control Sci Technol* 2017; 3: 171–201.

[+ Show References](#)[Crossref](#)[Google Scholar](#)

---

4. Stengel RF. *Optimal control and estimation*. New York: Dover Publications, 1994.

[Go To Reference](#)[Google Scholar](#)

---

5. Chauvin J, Moulin P, Corde G, Petit N, Rouchon P. Kalman filtering for real-time individual cylinder air fuel ratio observer on a diesel engine test bench. In: Proceedings of the American control conference, Minneapolis, MN, 14–16 June 2006. New York: IEEE.

[Go To Reference](#)[Google Scholar](#)

6. Tschanz F, Amstutz A, Onder CH, Guzzella L. Feedback control of particulate matter and nitrogen oxide emissions in diesel engines. *Control Eng Pract* 2013; 21(12): 1809–1820.

[Go To Reference](#)

[Crossref](#)

[Google Scholar](#)

- 
7. Hsieh M-F, Wang J. Design and experimental validation of an extended Kalman filter-based NOx concentration estimator in selective catalytic reduction system applications. *Control Eng Pract* 2011; 19(4): 346–353.

[Go To Reference](#)

[Crossref](#)

[Google Scholar](#)

- 
8. Guardiola C, Pla B, Blanco-Rodriguez D, Eriksson L. A computationally efficient Kalman filter based estimator for updating look-up tables applied to NOx estimation in diesel engines. *Control Eng Pract* 2013; 21(11): 1455–1468.

[Go To Reference](#)

[Crossref](#)

[Web of Science](#)

[Google Scholar](#)

- 
9. Surenahalli HS, Parker GG, Johnson JH. Extended Kalman filter estimator for NH<sub>3</sub> storage, NO, NO<sub>2</sub> and NH<sub>3</sub> estimator in a SCR. SAE technical paper 2013-01-1581, 2013.

[Go To Reference](#)

[Google Scholar](#)

10. Surenahalli HS, Parker GG, Johnson JH, Devarakonda MN. A Kalman filter estimator for a diesel oxidation catalyst during active regeneration of a CPF. In: Proceedings of the American control conference, Montreal, QC, 27–29 June 2012. New York: IEEE.

[Go To Reference](#)

[Google Scholar](#)

- 
11. Surenahalli HS, Parker GG, Johnson JH. Extended Kalman filter to estimate NO, NO<sub>2</sub>, hydrocarbon and temperatures in a DOC during active regeneration and under steady state conditions. SAE technical paper 2015-01-1059, 2015.

[+ Show References](#)

[Google Scholar](#)

- 
12. Surenahalli HS. *Dynamic model based state estimation in a heavy duty diesel aftertreatment system for onboard diagnostics and controls*. PhD Dissertation, Michigan Technological University, Houghton, MI, 2013.

[+ Show References](#)

[Google Scholar](#)

- 
13. Mahadevan BS, Johnson JH, Shahbakhti M. Experimental and simulation analysis of temperature and particulate matter distribution for a catalyzed diesel particulate filter. *J Emiss Control Sci Technol* 2015; 1: 255–283.

[Go To Reference](#)

[Crossref](#)

[Google Scholar](#)

- 
14. Du Y, Hu G, Xiang S, Zhang K, Liu H, Guo F. Estimation of the diesel particulate filter soot based on an equivalent circuit model. *Energies* 2018; 11: 472.

[Go To Reference](#)[Crossref](#)[Google Scholar](#)

- 
15. Shiel KL, Naber J, Johnson JH, Hutton CR. Catalyzed particulate filter passive oxidation study with ULSD and biodiesel blended fuel. SAE technical paper 2012-01-0837, 2012.

[+ Show References](#)[Google Scholar](#)

- 
16. Pidgeon J, Johnson JH, Naber J. An experimental investigation into particulate matter oxidation in a catalyzed particulate filter with biodiesel blends on an engine during active regeneration. SAE technical paper 2013-01-0521, 2013.

[+ Show References](#)[Google Scholar](#)

- 
17. Mahadevan BS. *Development of a multi-zone catalyzed particulate filter model and Kalman filter estimator for simulation and control of particulate matter distribution of a CPF for engine ECU applications*. PhD Dissertation, Michigan Technological University, Houghton, MI, 2017.

[+ Show References](#)[Google Scholar](#)

- 
18. Konstandopoulos AG, Johnson JH. Wall-flow diesel particulate filters—their pressure drop and collection efficiency. SAE technical paper 890405, 1989.



[Go To Reference](#)[Crossref](#)[Google Scholar](#)

---

19. Çengel YA. *Heat and mass transfer: a practical approach*. 3rd ed., Chapter 5, pp.311–334. New Delhi: Tata McGraw-Hill Publication, 2008.

[Go To Reference](#)[Google Scholar](#)

---

20. Continental-automotive.com. Medium/heavy duty engine control unit. <https://www.continental-automotive.com/en-gl/Trucks-Buses/Powertrain/Diesel-Vehicles/Engine-Management/Medium-Heavy-Duty-Engine-Control-Unit> (accessed 1 July 2018).

[Go To Reference](#)[Google Scholar](#)

---

21. Depcik C, Assanis DN. Graphical user interfaces in an engineering educational environment. *Comput Appl Eng Educ* 2005; 13(1): 48–59.

[Go To Reference](#)[Crossref](#)[Google Scholar](#)

---

22. Haralampous OA, Koltsakis GC. Back-diffusion modeling of NO<sub>2</sub> in catalyzed diesel particulate filters. *Ind Eng Chem Res* 2004; 43: 875–883.

[Go To Reference](#)[Crossref](#)

[Web of Science](#)[Google Scholar](#)

- 
23. Premchand KC, Surenahalli H, Johnson JH. Particulate matter and nitrogen oxides based on engine experimental data for a catalyzed diesel particulate filter. SAE technical paper 2014-01-1553, 2014.

[Go To Reference](#)[Google Scholar](#)

- 
24. Haralampous OA, Koltsakis GC, Samaras ZC, Vogt C-D, Ohara E, Watanabe Y, Mizutani T. Reaction and diffusion phenomena in catalyzed diesel particulate filters. SAE technical paper 2004-01-0696, 2004.

[+ Show References](#)[Google Scholar](#)

- 
25. Depcik C, Langness C, Mattson J. Development of a simplified diesel particulate filter model intended for an engine control unit. SAE technical paper 2014-01-1559, 2014.

[Go To Reference](#)[Google Scholar](#)

- 
26. Koltsakis GC, Haralampous OA, Margaritis NK, Samras ZC, Vogt C-D, Ohara E, et al. 3-dimensional modeling of the regeneration in SiC particulate filters. SAE technical paper 2005-01-0953, 2005.

[Go To Reference](#)[Google Scholar](#)

---

Simon D. *Optimal state estimation: Kalman, H infinity and non-linear approaches*. Chapter 13, pp.400–409. Hoboken, NJ: John Wiley & Sons, 2006.

[+ Show References](#)[Crossref](#)[Google Scholar](#)

---

28. Simon D. *Optimal state estimation: Kalman, H infinity and non-linear approaches*. Chapter 15, pp.461–481. Hoboken, NJ: John Wiley & Sons, 2006.

[+ Show References](#)[Crossref](#)[Google Scholar](#)

---

29. Kim P. *Kalman filter for beginners with MATLAB examples*. La Vergne: CreateSpace, 2011.

[Go To Reference](#)[Google Scholar](#)

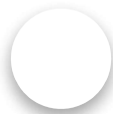
---

30. Simon D. *Optimal state estimation: Kalman, H infinity and non-linear approaches*. Chapter 5, pp.139–145. Hoboken, NJ: John Wiley & Sons, 2006.

[Go To Reference](#)[Crossref](#)[Google Scholar](#)

---

31. Ranalli M, Hossfeld C, Kaiser R, Schmidt S, Elfinger G. Soot loading distribution as a key factor for a reliable DPF system: an innovative development methodology. SAE technical paper 2002-01-2158, 2002.



[Go To Reference](#)[Google Scholar](#)

32. Gong J, Stewart ML, Zelenyuk A, Strzelec A, Viswanathan S, Rothamer DA, et al. Importance of filter's microstructure in dynamic filtration modeling of gasoline particulate filters (GPFs): inhomogeneous porosity and pore size distribution. *Chem Eng J* 2018; 338: 15–26.

[+ Show References](#)[Crossref](#)[Google Scholar](#)

33. Pidgeon J. *An experimental investigation into the effects of biodiesel blends on particulate matter oxidation in a catalyzed particulate filter during active regeneration*. Master's Thesis, Michigan Technological University, Houghton, MI, 2013.

[Google Scholar](#)

## Supplementary Material

Please find the following supplemental material available below.

For Open Access articles published under a [Creative Commons License](#), all supplemental material carries the same license as the article it is associated with.

For non-Open Access articles published, all supplemental material carries a non-exclusive license, and permission requests for re-use of supplemental material or any part of supplemental material shall be sent directly to the copyright owner as specified in the copyright notice associated with the article.

 [ijer-18-0031-r2-supplementary\\_appen](#) 529.88 KB  


Similar articles:

 Restricted access

[Development of a Kalman filter estimator for simulation and control of NO<sub>x</sub> and PM in a SCR catalyst on a DPF](#)

Show Details ▾



Restricted access

[A review of the literature of selective catalytic reduction catalysts integrated into diesel particulate filters](#)

Show Details ▾



Open Access

[Diesel particulate filter design simulation: A review](#)

Show Details ▾

[View More](#)

Sage recommends:

**SAGE Knowledge**

Entry

[Kinetic \(Molecular\) Theory](#)

Show Details ▾

**SAGE Knowledge**

Literature review

[Understanding the Kalman Filter](#)

Show Details ▾

**SAGE Knowledge**

Entry

[Atmospheric Pressure](#)

Show Details ▾



[View More](#)

## Also from Sage

### CQ Library

Elevating debate

### Sage Data

Uncovering insight

### Sage Business Cases

Shaping futures

### Sage Campus

Unleashing potential

### Sage Knowledge

Multimedia learning resources

### Sage Research Methods

Supercharging research

### Sage Video

Streaming knowledge

### Technology from Sage

Library digital services

